Electronic Supplementary Information

Spin–induced electron transfer simultaneously enhancing intrinsic activity and stability of amorphous MoS_x–based materials toward efficient hydrogen evolution

Rui–Yuan Li [a], Yu–Xin Guo [b], Xiao–Yu Yang [b], Zhan Liu [b], Xiao–Yun Li [c], Yu Li [b], Yi–Yong Huang [a], Jin–Ping Liu [a], Shen Yu [b], Ming–Hui Sun [b], Li–Hua Chen [b,*], Bao–Lian Su [b, d,*], Yi–Long Wang [a,*]

[a] School of Chemistry, Chemical Engineering and Life Science, Wuhan University of Technology, Wuhan, Hubei 430070, China

[b] State Key Laboratory of Advanced Technology for Materials Synthesis and Processing, Wuhan University of Technology, Wuhan, Hubei 430070, China

[c] State Key Laboratory of Silicate Materials for Architectures, Wuhan University of Technology, Wuhan, Hubei 430070, China

[d] Laboratory of Inorganic Materials Chemistry (CMI), University of Namur 61 rue de Bruxelles Namur 5000, Belgium

*** Corresponding author: Prof. Li–Hua Chen (chenlihua@whut.edu.cn);**
Prof. Bao–Lian Su (baoliansu@whut.edu.cn);
Prof. Yi–Long Wang (wangyilong@whut.edu.cn).

Contents

Experimental Section

1.1 Treatment of carbon cloth (CC)

A piece of CC with a size of 2.0 × 2.5 cm^2 was scanned by cyclic voltammetry (CV) six times at a scanning rate of 20.0 mV s^{-1} in 2.0 mol L^{-1} H_2SO_4 solution. Graphite and saturated calomel electrodes were used as counter and reference electrodes, respectively. The electrochemical potentials windows at the anode were set from 1.0 to 1.8 V. After electrochemical oxidation, the treated CC was cleaned by ultrasonic with deionized water and ethanol for 10.0 min. Then, it was dried in a vacuum drying oven at 60.0 °C for 3.0 h.

1.2 Characterization

The phase structures of all samples were examined by using powder X-ray diffraction (XRD) patterns using a Bruker AXS D8-Advance, a diffractometer with Cu Ka radiation (λ= 0.15418 nm) in the 2θ range from 10° to 70° at a scanning step of 0.05°. A micro-Raman study was performed on the Renishaw in Via (Britain) laser confocal Raman microscope at room temperature under an excitation wavelength of 633 nm with He-Ne laser. The high-resolution TEM (HRTEM) images as well as the corresponding selected area electron diffraction (SAED) patterns of the samples were further investigated by a JEOL JEM-2100F HRTEM, and the accelerating voltage was 200 kV. Before TEM analysis, these samples were prepared by depositing a single drop of diluted sample dispersion in ethanol onto a copper grid coated with an amorphous

carbon film. X-ray photoelectron spectroscopy (XPS) measurements were employed by a VG Multilab 2000 X XPS system equipped with the Al Ka source. All the binding energies were referenced to the C1s peak at 284.8 eV of the surface adventitious carbon. Morphologies of all samples were observed by a field emission scanning electron microscopy (FESEM; Hitachi S-4800) operated at an accelerating voltage of 5.0 kV. Scanning TEM (STEM) - energy-dispersive X-ray spectroscopy (EDX) spectrum was recorded with an EDX attached to HRTEM. Elemental mapping results of Co-MoS_x/CC-0.4 were acquired by the high-angle annular dark-field scanning transmission electron microscopy (HAADF-STEM) mode in combination with energy-dispersive X-ray spectroscopy (EDX) analysis. The X-ray absorption spectroscopy (XAFS) study was performed at the BL08B2* of SPring-8 (8 GeV, 100 mA), Japan, in which, the X-ray beam was mono-chromatized with water-cooled Si (111) double-crystal monochromator and focused with two Rh coated focusing mirrors with the beam size of 2.0 mm in the horizontal direction and 0.5 mm in the vertical direction around sample position, to obtain X-ray adsorption fine structure (XAFS) spectra both in near and extended edge. Mo foil, MoS_2, MoO_2, Co foil, CoS_2 and Co_3O_4 samples were used as references. Electron paramagnetic resonance (EPR) spectra were measured using Bruker EMX PLUS EPR spectrometer. The samples were placed in a rectangular resonate at 9.838960 GHz. The magnetic properties of the samples were tested using a vibrating sample magnetometer (VSM) (Lakeshore 7404, LakeShore, USA) at the room

temperature. Magnetic hysteresis loops were recorded in a magnetic field within 2.17 T.

1.3 Electrochemical measurements

Electrochemical measurements were carried out in a standard three-electrode system on a CHI 660E electrochemical workstation (Shanghai Chenhua Instruments, China) at room temperature with as-obtained samples (area: 0.5 × 0.5 cm^2) as the working electrode, a graphite rod as the counter electrode, and a saturated calomel electrode (SCE) (saturated KCl solution) as the reference electrode. All experiments were done in the electrolyte of 0.5 M H_2SO_4 bubbled with N_2. Unless otherwise specified, all potentials in electrochemical measurements were converted to the potentials *versus* the reversible hydrogen electrode (RHE) by Supplementary Equation 01:

$$E(vs\ RHE) = E(vs\ SCE) + 0.059 \times pH + 0.241V \quad (01)$$

For HER measurements, line sweep voltammetry (LSV) was measured at a scan rate of 5.0 mV s^{-1} without the additional compensations. Polarization curves were recorded between 0 and -0.40 V (vs RHE). Tafel slopes were calculated from the polarization curves. Nyquist plots were measured with frequencies ranging from 100 kHz to 0.01 Hz at a potential of -0.001 V (vs RHE). The impedance data were fitted to a simplified Randles circuit to extract the series and charge-transfer resistance. Mott-Schottky plots were measured at a same frequency between 0.0 and 1.0 V (vs RHE). For the investigation of electrochemical double-layer capacitances (C_{dl}), cyclic voltammetry (CV) was

measured at the scan rates of 70.0, 80.0, 90.0, 100.0, 110.0 and 120.0 mV s^{-1}, respectively, in the potential ranging from -0.1 to -0.2 V (vs RHE). Chronoamperometric responses (*i*~*t*) methods were conducted to record the long-term durability. Also, the cycling performance of the electrode was assessed by repeating linear sweep voltammetry for 1000 cycles in the potential window of −0.5 to +0.1 V versus RHE at a scan rate of 50 mV s^{-1}.

All the experiments were carried out and done at room temperature.

1.4 Calculation method

First-principle calculations were performed by the density functional theory (DFT) using the Vienna Ab-initio Simulation Package (VASP) package[1]. The generalized gradient approximation (GGA) with the Perdew-Burke-Ernzerhof (PBE) functional were used to describe the electronic exchange and correlation effects[2-4]. Uniform G-centered k-points meshes with a resolution of 2π*0.05 $Å^{-1}$ and Methfessel-Paxton electronic smearing were adopted for the integration in the Brillouin zone for geometric optimization. The simulation was run with a cutoff energy of 500 eV throughout the computations. These settings ensure convergence of the total energies to within 1 meV per atom. Structure relaxation proceeded until all forces on atoms were less than 10 meV $Å^{-1}$ and the total stress tensor was within 0.03 GPa of the target value. A vacuum distance of 15 Å was set to ensure sufficient vacuum and avoid interactions between two periods. The DFT-D2 Van der Walls correction by Grimme was also considered in all calculations[5,6].

The free energy of the adsorption atomic hydrogen (ΔG_{H^*}) is obtained by：

$$\Delta G_{H^*} = \Delta E_{H^*} + \Delta E_{ZPE} - T\Delta S_{H^*}$$

ΔE_{H^*} describes the energy needed to increase the coverage by one hydrogen atom. ΔE_{ZPE} is the difference in zero point energy and ΔS_{H^*} is the difference in entropy. ΔE_{ZPE} - $T\Delta S_{H^*}$ is about 0.24 eV, so $\Delta G_{H^*} = \Delta E_{H^*} + 0.24$[5]. For ΔE_{H^*}, it is calculated as follows:

$$\Delta E_{H^*} = E(\text{Surface} + H^*) - E(\text{Surface}) - 1/2E(H_2)$$

Where E(surface+H*) represents the total energy of the selected surfaces with one adsorbed hydrogen atom on the surfaces, E(surface) represents the total energy of the surfaces, while $E(H_2)$ represents the total energy of a gas phase H_2 molecule.

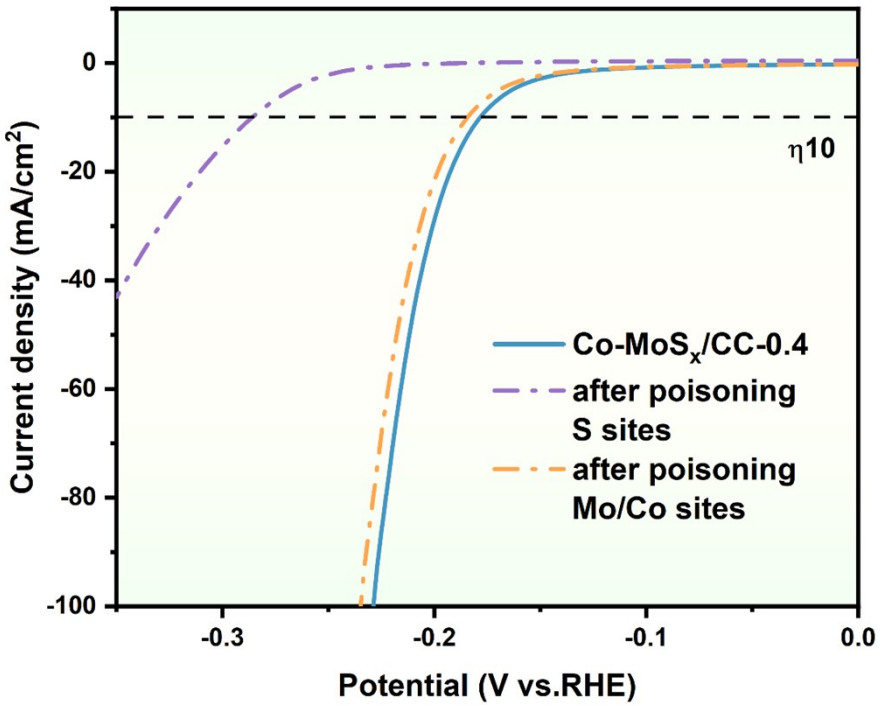

Fig. S1 Polarization curves of Co–MoS_x/CC–0.4 before–and–after poisoning S, Mo and Co sites.

The experimental steps about poisoning Mo and Co sites are follows: the electrochemical tests are performed in 0.5 mol L^{-1} H_2SO_4 containing 10 mmol L^{-1} SCN^-.

The experimental steps about poisoning S sites are follows: Co–MoS_x/CC–0.4 is incubated for 90.0 h in a fresh solution of 10.0 mL of chloroform and 0.3 mL of dodecanethiol. After being taken from the thiol solutions, the related sample is washed with ethanol and dried in air. Then, the HER activity is further tested in 0.5 mol L^{-1} H_2SO_4.

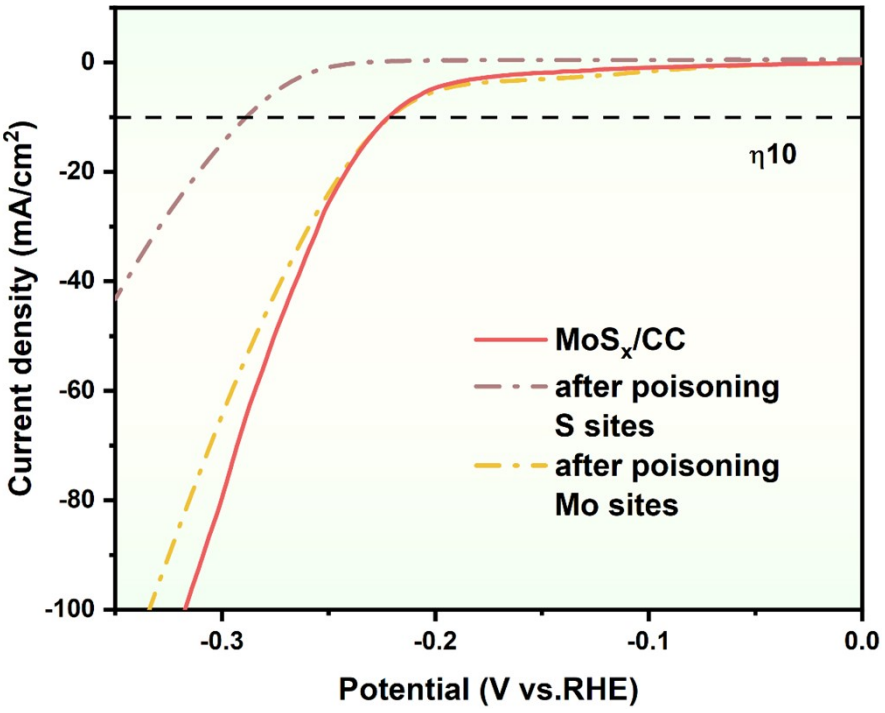

Fig. S2 Polarization curves of MoS_x/CC before and after poisoning S and Mo sites.

The experimental steps about poisoning Mo sites are follows: the electrochemical tests are performed in 0.5 mol L^{-1} H_2SO_4 containing 10 mmol L^{-1} SCN^-.

The experimental steps about poisoning S sites are follows: MoS_x/CC is incubated for 90.0 h in a fresh solution of 10.0 mL of chloroform and 0.3 mL of dodecanethiol. After being taken from the thiol solutions, the related sample is washed with ethanol and dried in air. Then, the HER activity is further tested in 0.5 mol L^{-1} H_2SO_4.

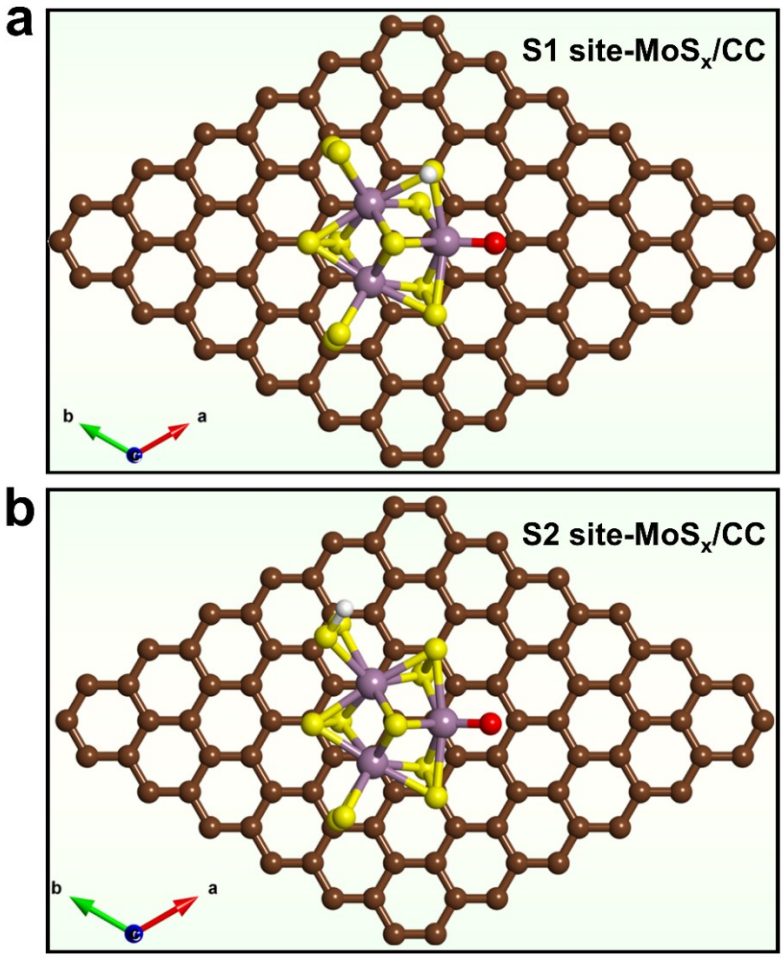

Fig. S3 Schematic illustration of MoS_x/CC model for the adsorption of H* at (a) S1 and (b) S2 sites. Meanwhile, the purple, yellow, brown, red and white balls represent Mo, S, C, O and H atoms, respectively.

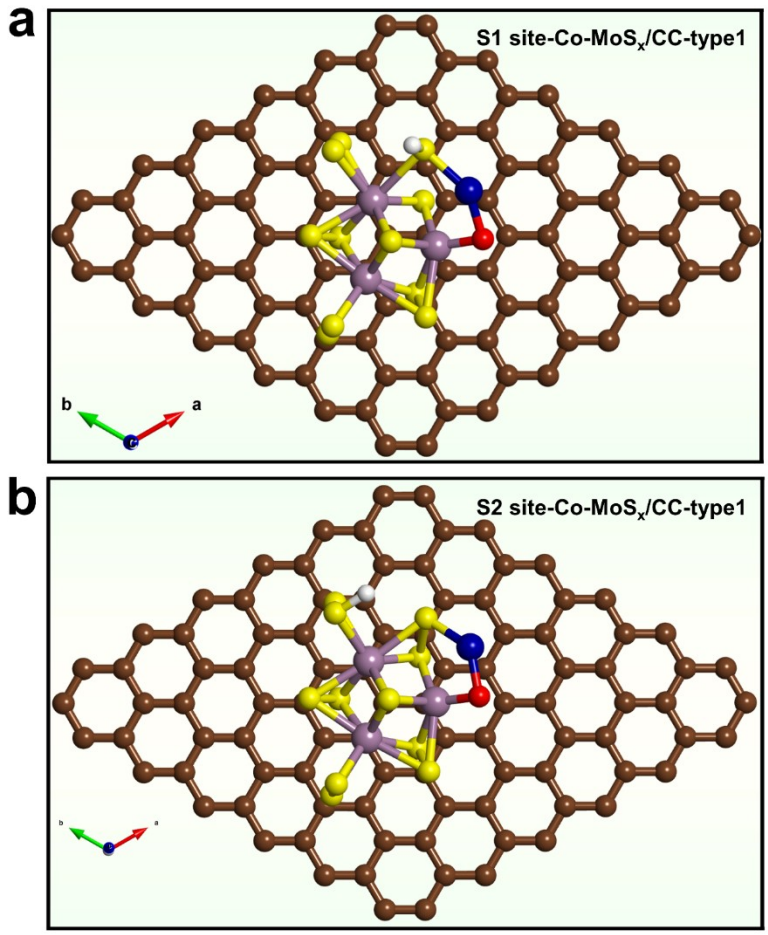

Fig. S4 Schematic illustration of Co–MoS_x/CC–type1 model for the adsorption of H* at (a) S1 and (b) S2 sites. Meanwhile, the purple, yellow, blue, brown, red and white balls represent Mo, S, Co, C, O and H atoms, respectively.

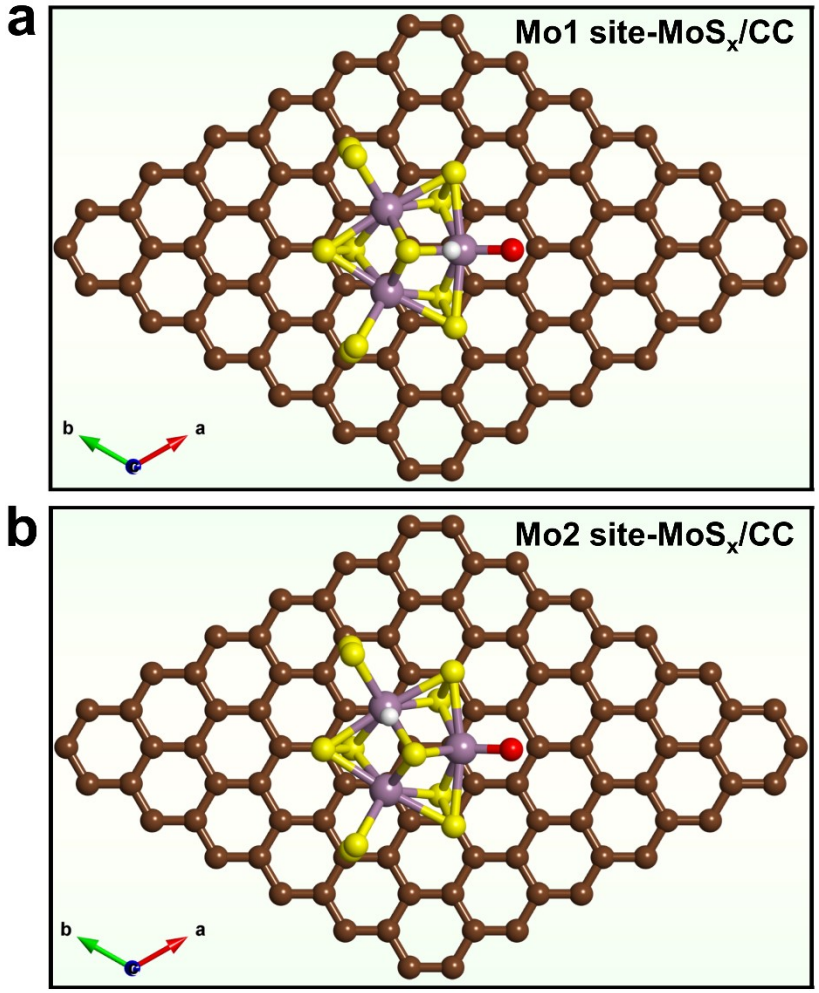

Fig. S5 Schematic illustration of MoS_x/CC model for the adsorption of H* at (a) Mo1 and (b) Mo2 sites. Meanwhile, the purple, yellow, brown, red and white balls represent Mo, S, C, O and H atoms, respectively.

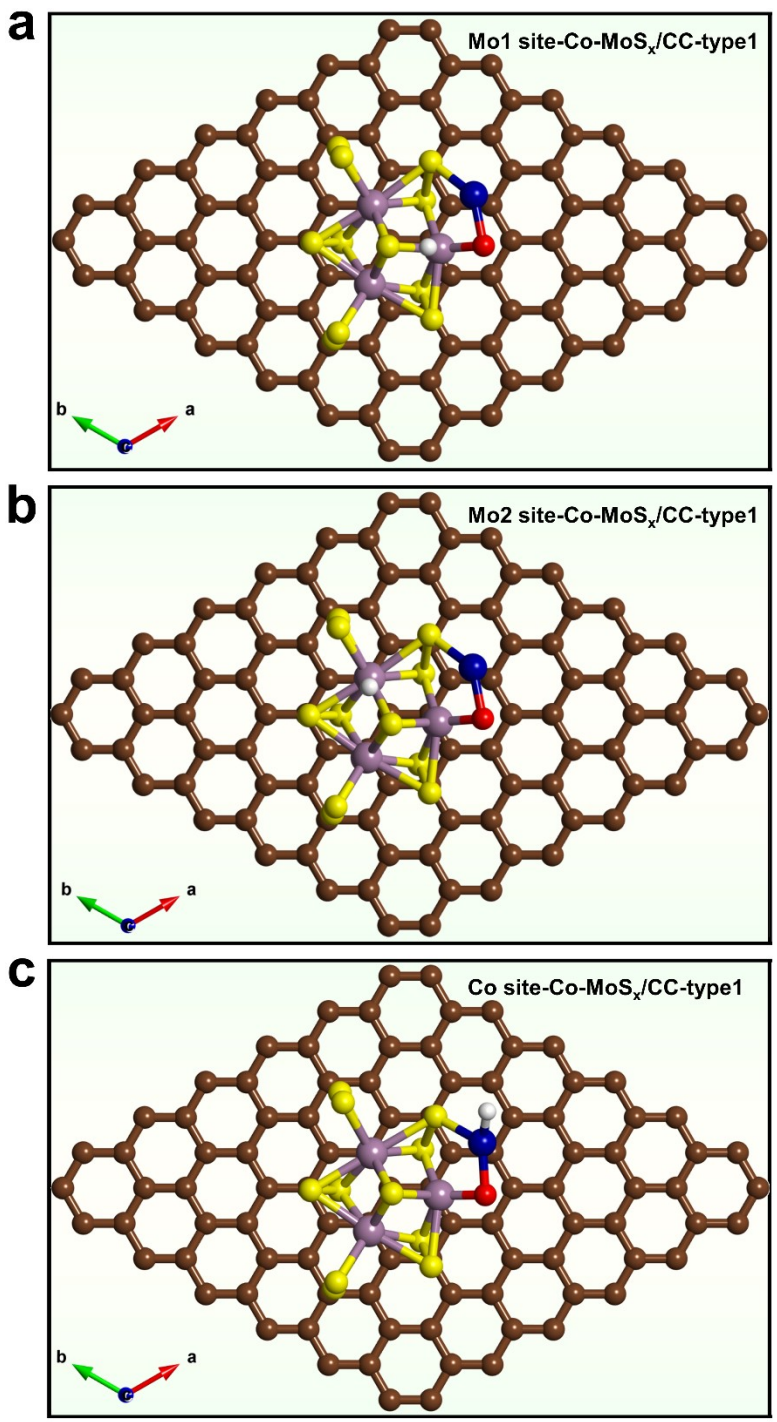

Fig. S6 Schematic illustration of Co–MoS_x/CC–type1 model for the adsorption of H* at (a) Mo1, (b) Mo2 and (c) Co sites. Meanwhile, the purple, yellow, blue, brown, red and white balls represent Mo, S, Co, C, O and H atoms, respectively.

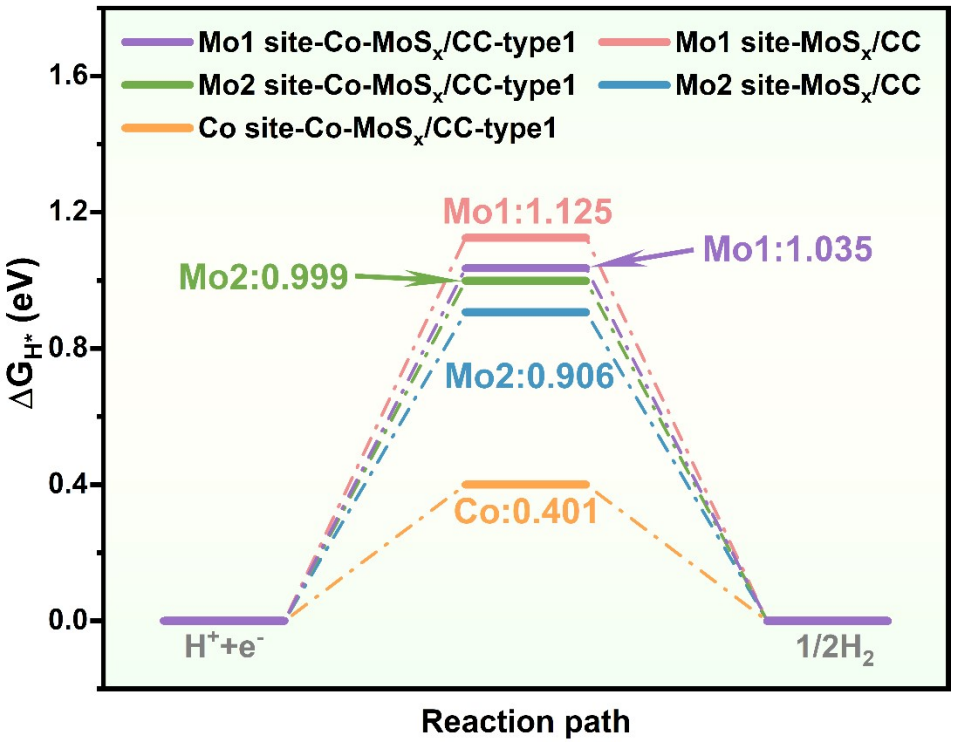

Fig. S7 ΔG_{H^*} at Mo1 and Mo2 sites of MoS_x/CC model as well as Mo1, Mo2 and Co sites of Co–MoS_x/CC–type1 model.

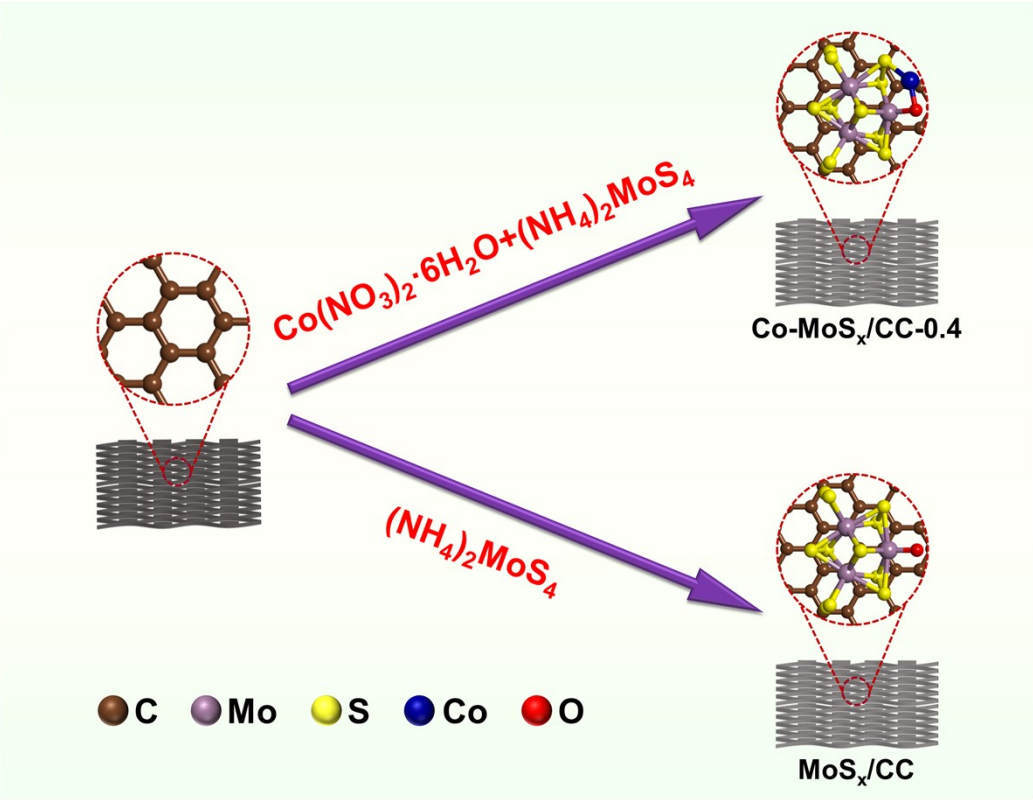

Fig. S8 Schematic illustration of the synthesis of MoS_x/CC and Co–MoS_x/CC–0.4 samples. Meanwhile, the purple, yellow, blue, brown and red balls represent Mo, S, Co, C and O atoms, respectively.

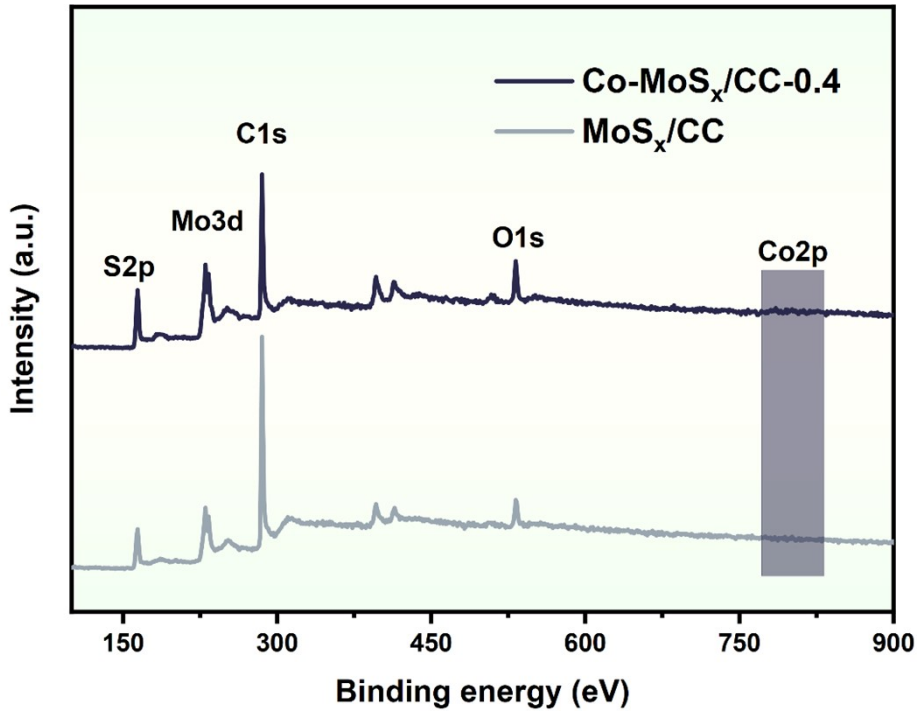

Fig. S9 Full XPS spectra of Co–MoS_x/CC–0.4 and MoS_x/CC.

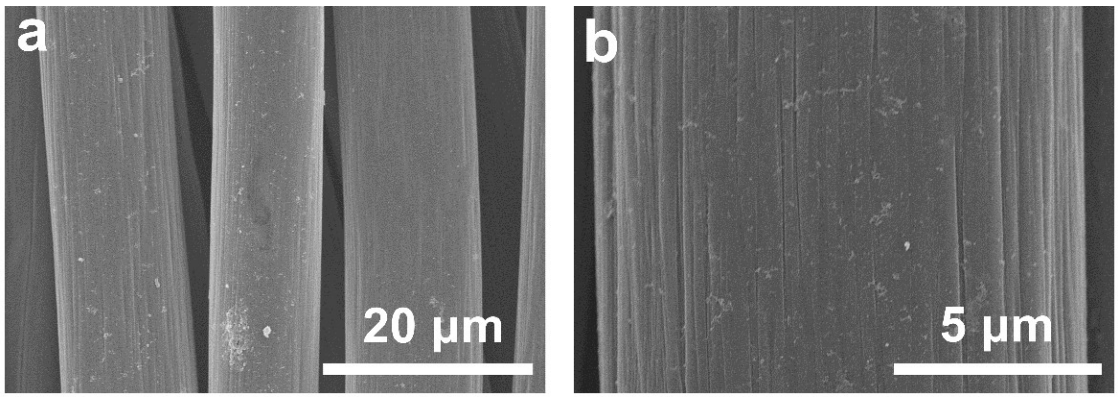

Fig. S10 SEM images of MoS_x/CC.

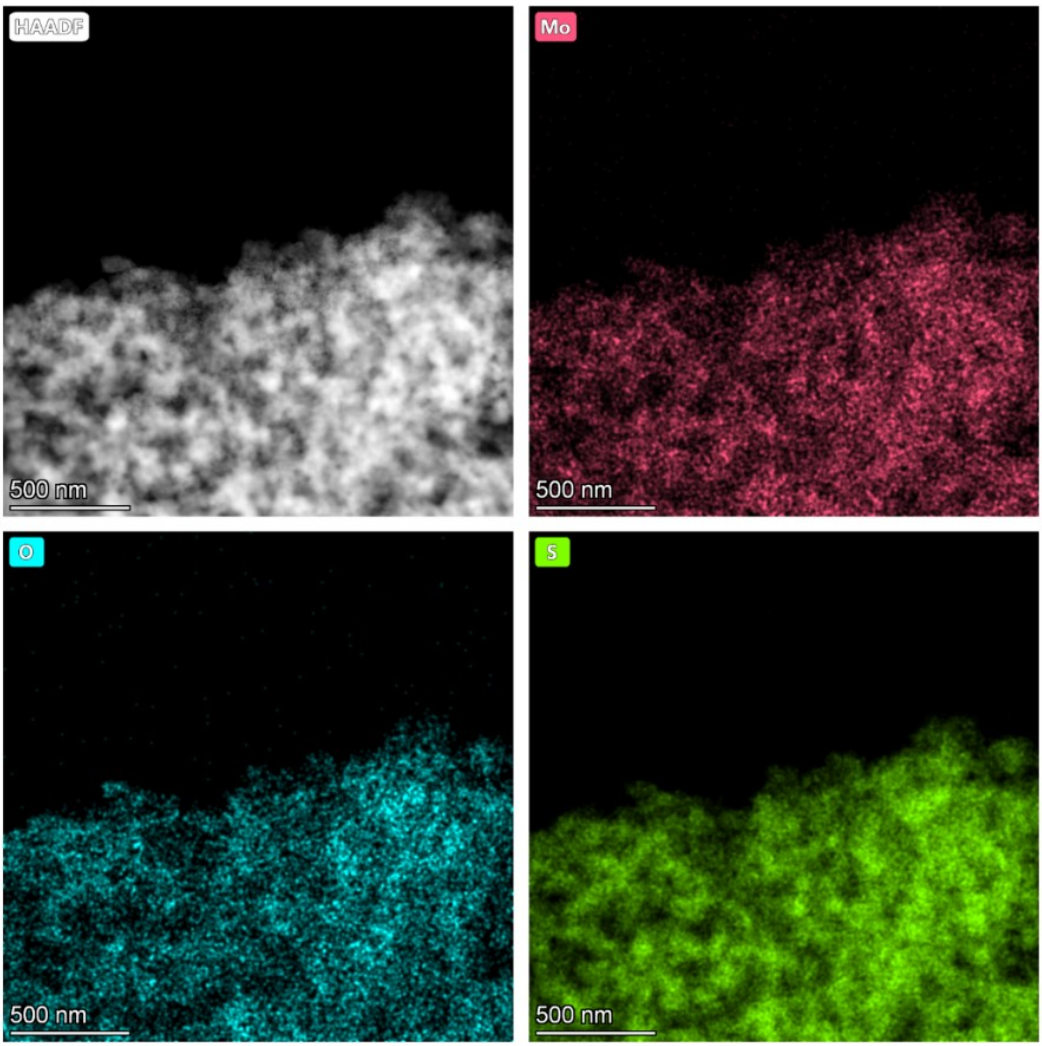

Fig. S11 HAADF-EDX mapping of Mo, S, Co and O over MoS_x.

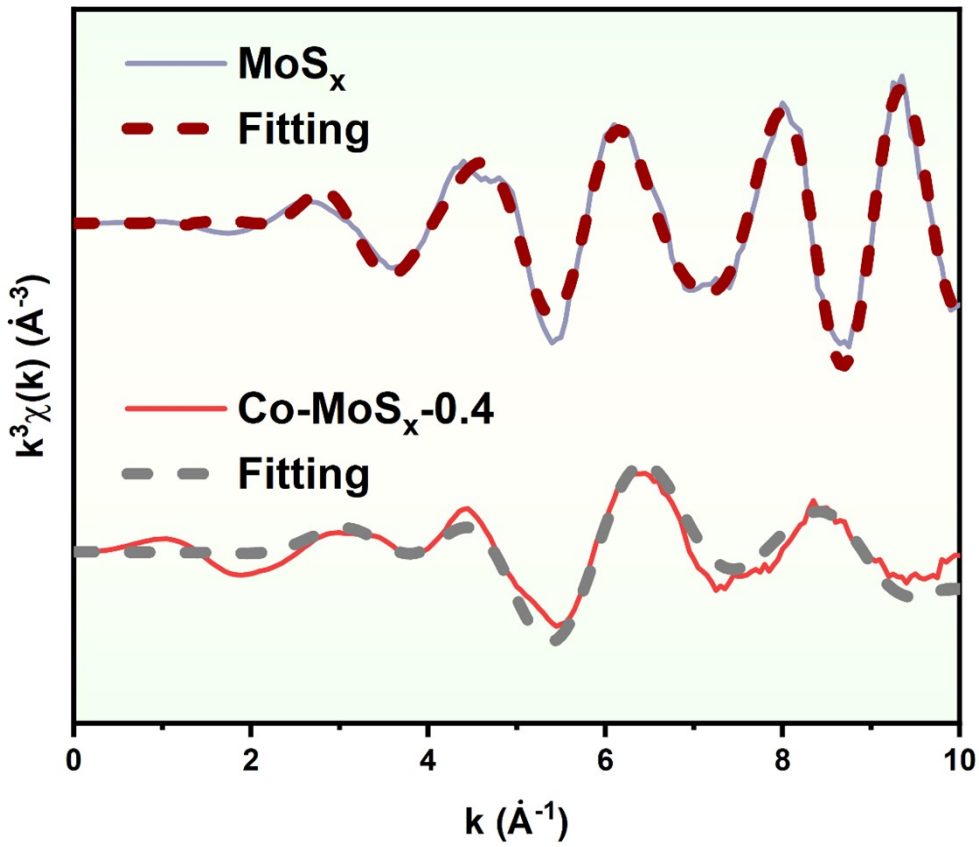

Fig. S12 Mo K-edge EXAFS oscillation function k^3 χ(k) and the corresponding fitting curves of MoS_x and Co–MoS_x–0.4.

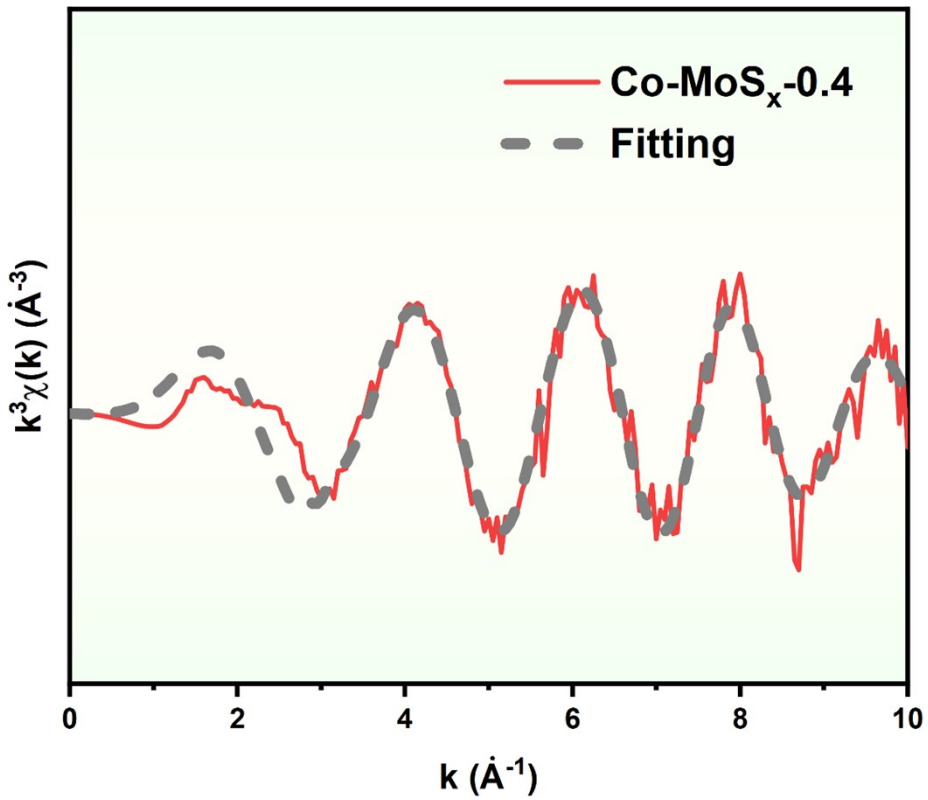

Fig. S13 Co K-edge EXAFS oscillation function k^3 χ(k) and the corresponding fitting curves of Co–MoS_x–0.4.

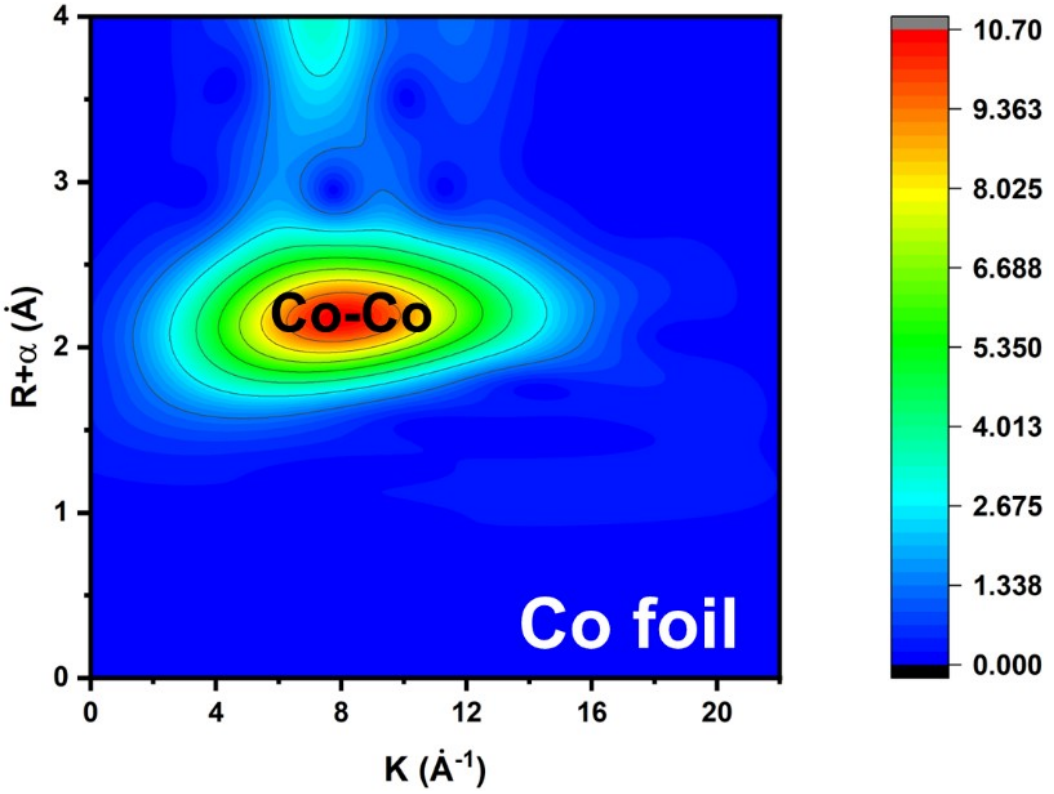

Fig. S14 Wavelet transform k^3-weighted Co K-edge EXAFS signals of Co foil.

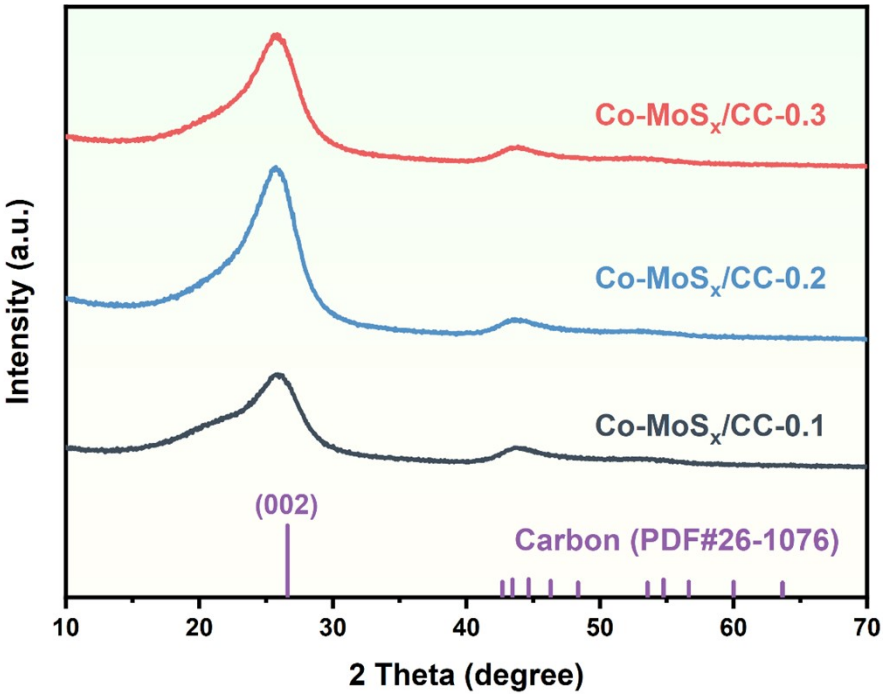

Fig. S15 XRD patterns of Co–MoS_x/CC–0.1, Co–MoS_x/CC–0.2 and Co–MoS_x/CC–0.3.

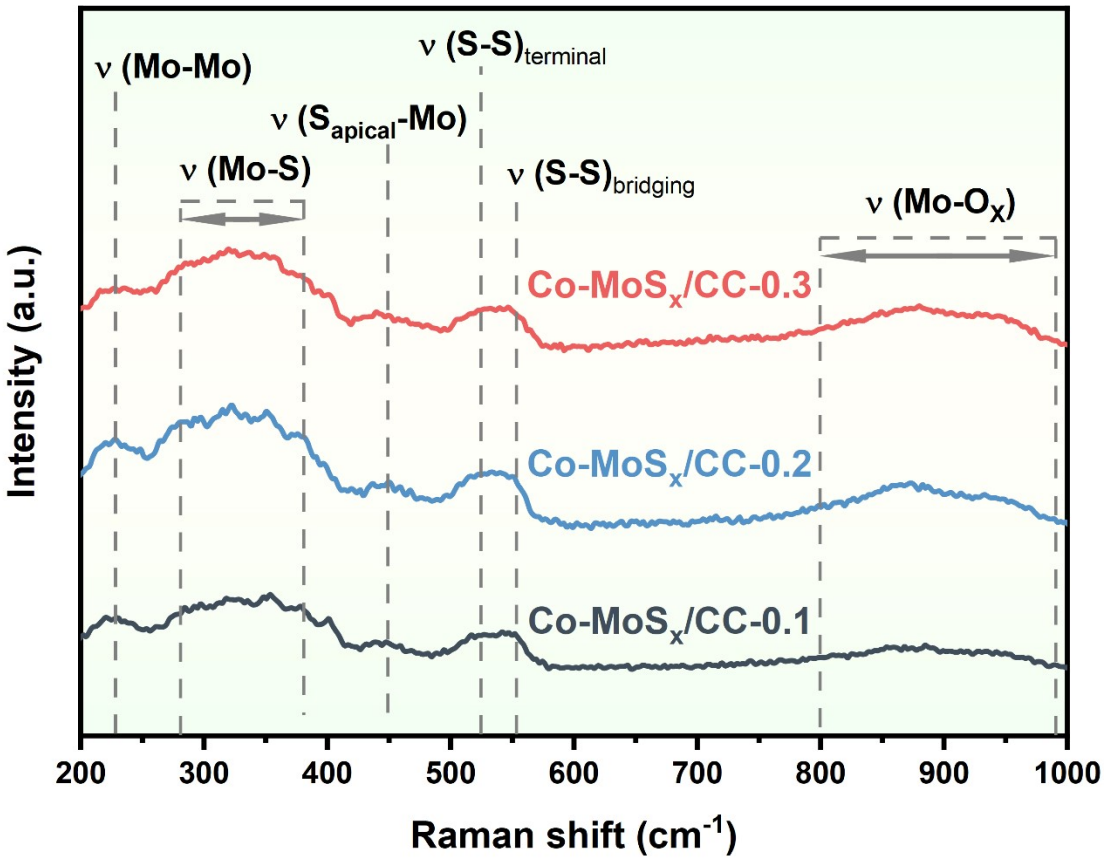

Fig. S16 Raman spectra of Co–MoS_x/CC–0.1, Co–MoS_x/CC–0.2 and Co–MoS_x/CC–0.3.

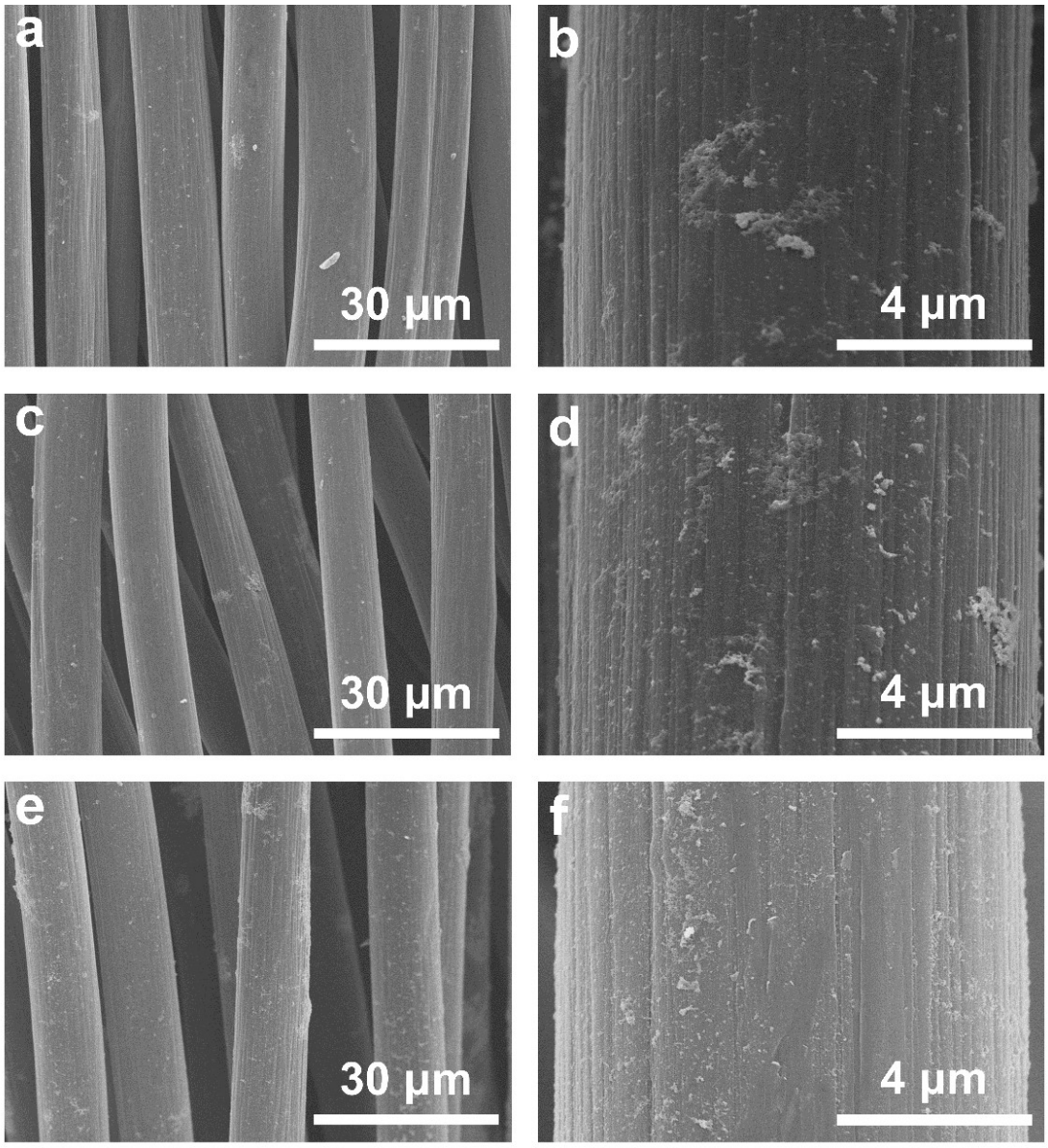

Fig. S17 SEM images of (a, b) Co–MoS_x/CC–0.1, (c, d) Co–MoS_x/CC–0.2 and (e, f) Co–MoS_x/CC–0.3.

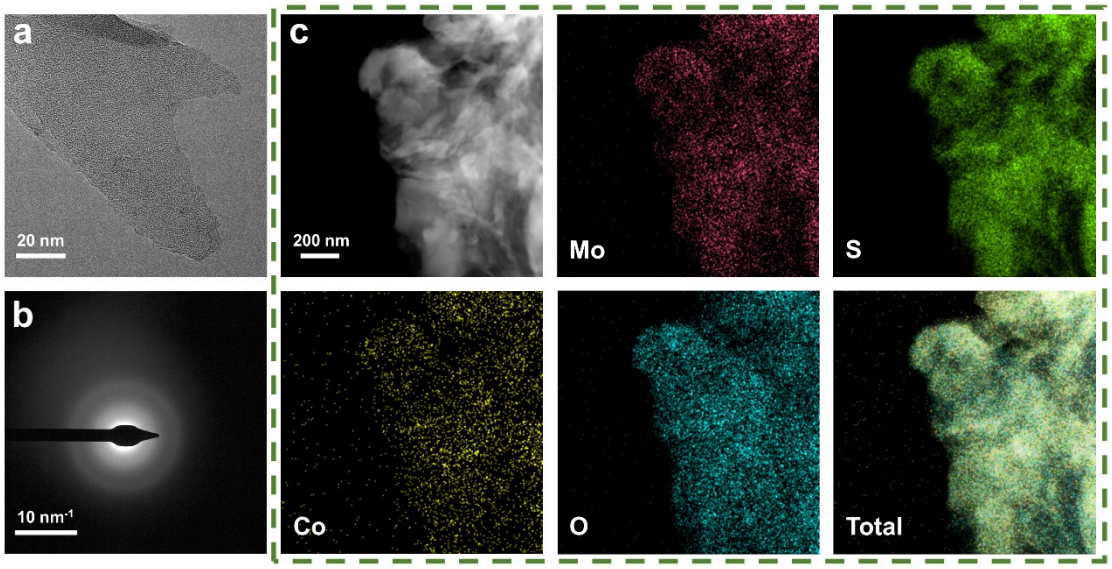

Fig. S18 (a) HRTEM image and (b) SAED pattern of Co–MoS_x–0.1; (c) HAADF-EDX mapping of Mo, S, Co and O over Co–MoS_x–0.1.

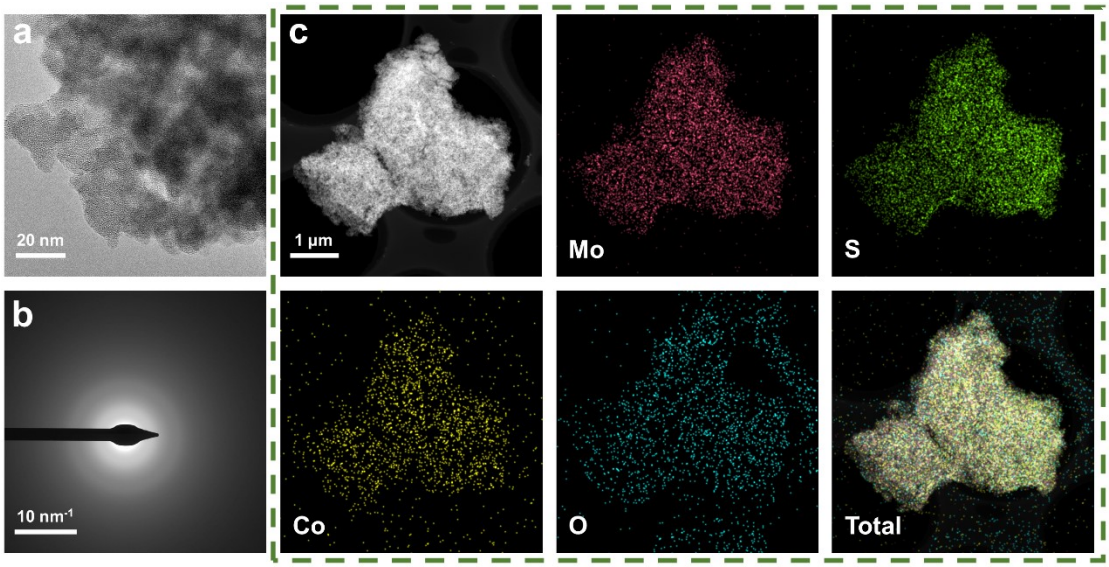

Fig. S19 (a) HRTEM image and (b) SAED pattern of Co–MoS_x–0.2; (c) HAADF-EDX mapping of Mo, S, Co and O over Co–MoS_x–0.2.

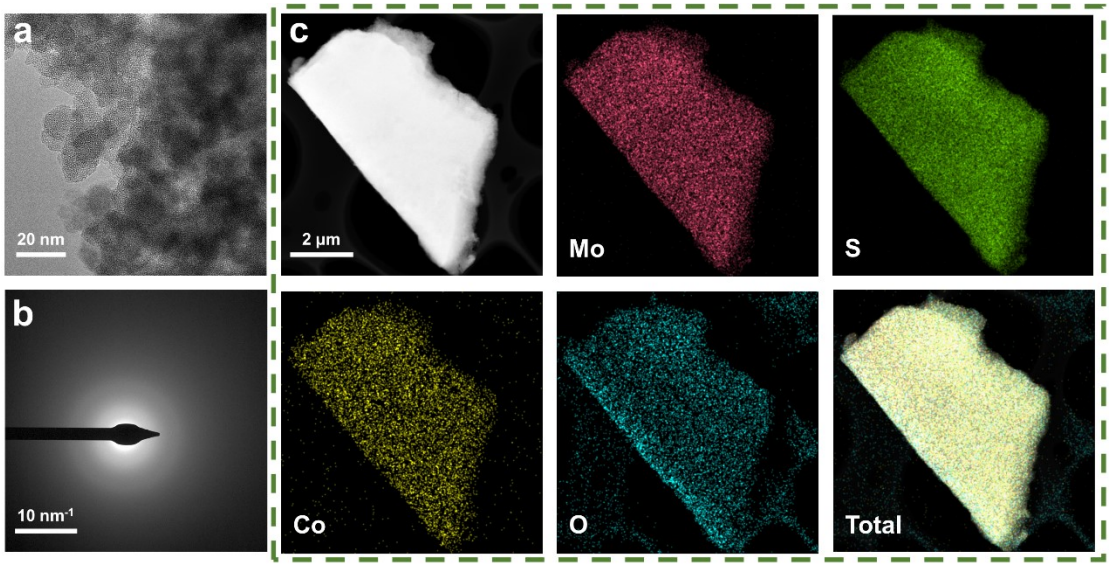

Fig. S20 (a) HRTEM image and (b) SAED pattern of Co–MoS_x–0.3; (c) HAADF-EDX mapping of Mo, S, Co and O over Co–MoS_x–0.3.

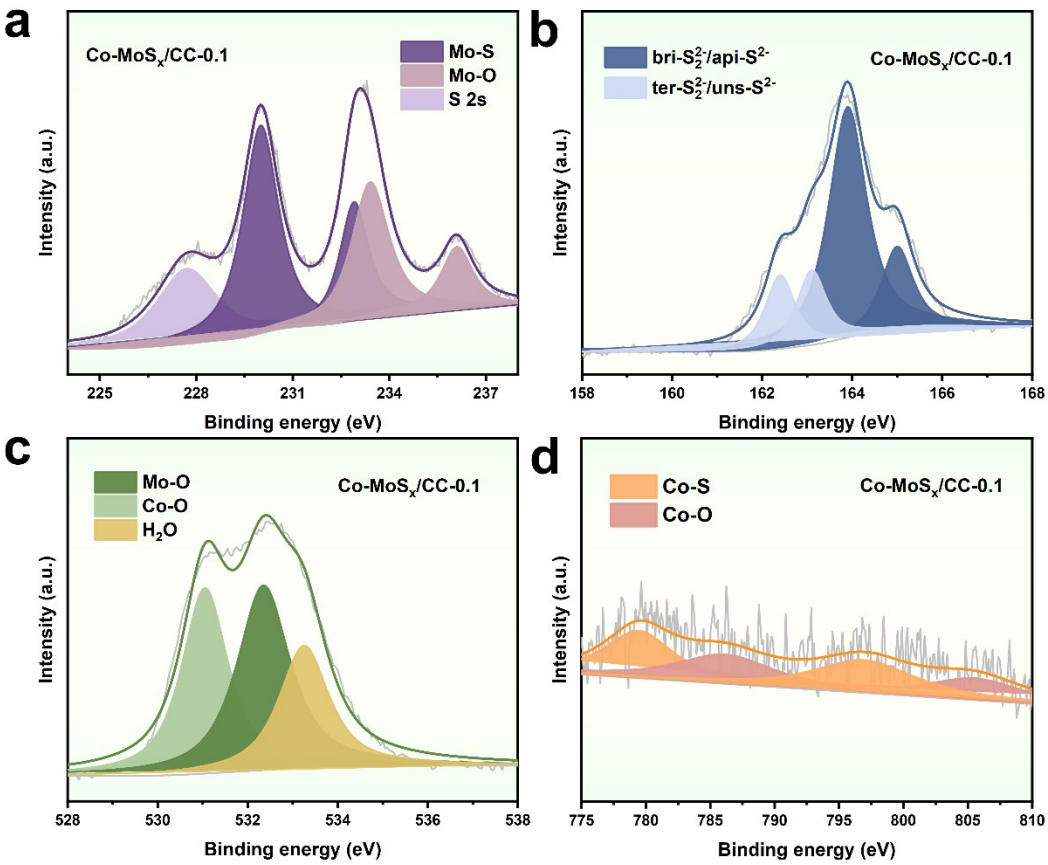

Fig. S21 (a) Mo3d, (b) S2p, (c) O1s and (d) Co2p XPS spectra of Co–MoS_x/CC–0.1.

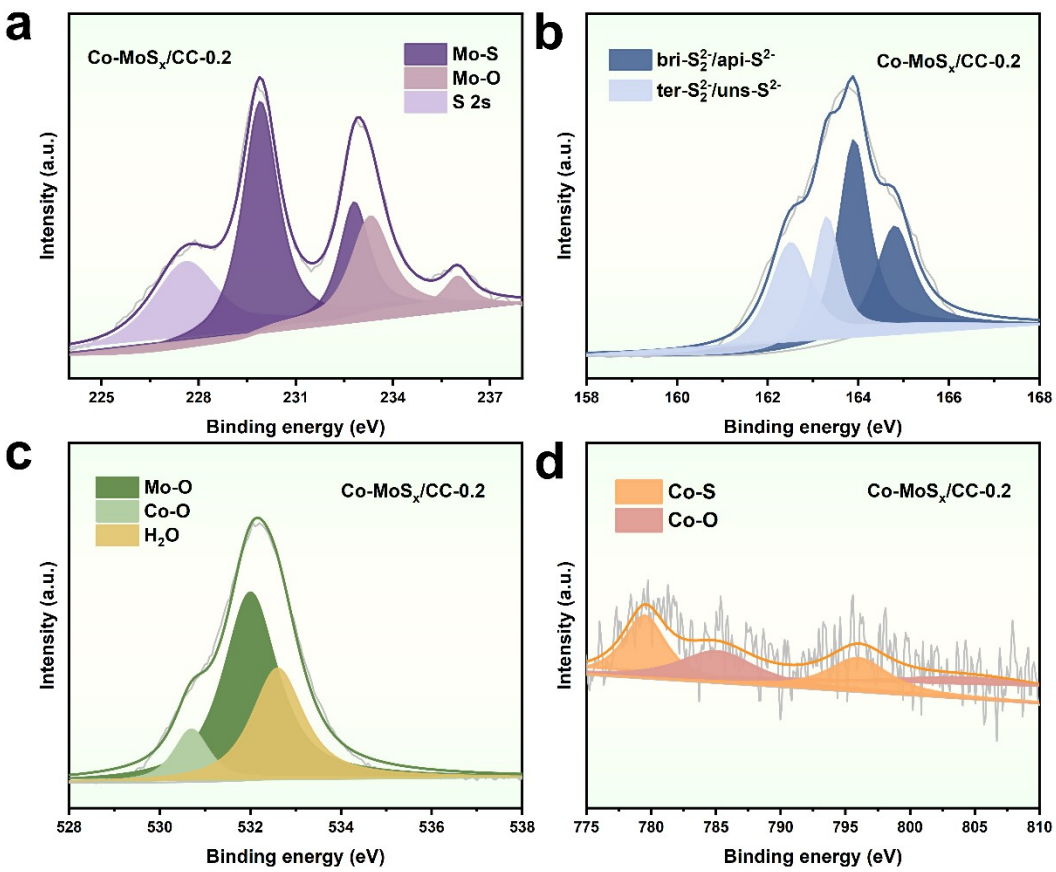

Fig. S22 (a) Mo3d, (b) S2p, (c) O1s and (d) Co2p XPS spectra of Co–MoS_x/CC–0.2.

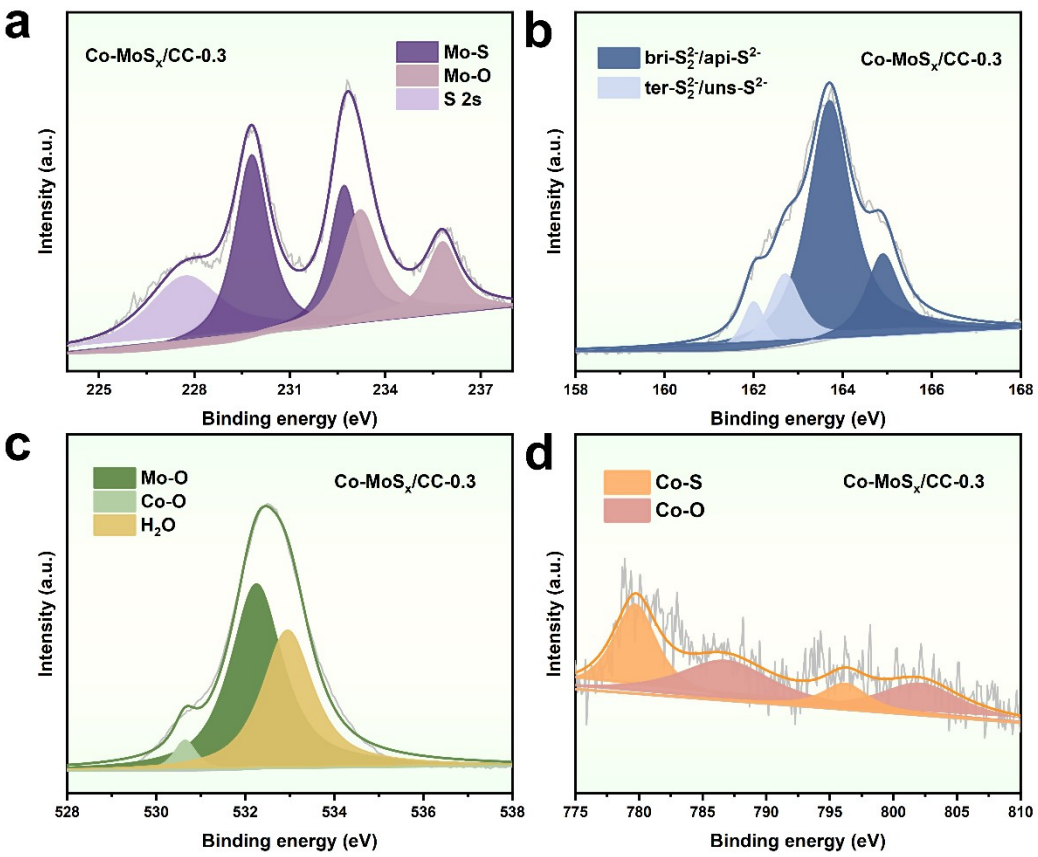

Fig. S23 (a) Mo3d, (b) S2p, (c) O1s and (d) Co2p XPS spectra of Co–MoS_x/CC–0.3.

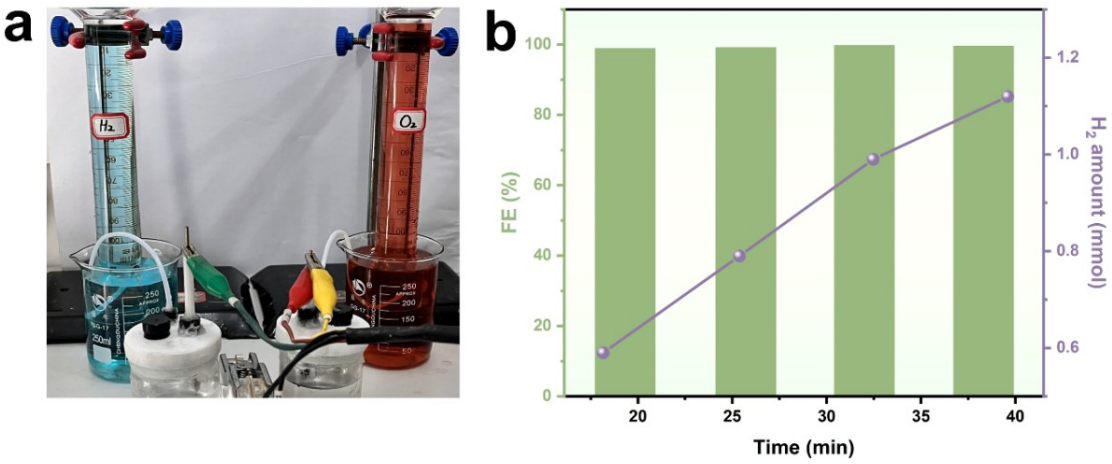

Fig. S24 (a) Photograph of the working electrode of Co–MoS_x/CC–0.4 for testing Faraday efficiency, (b) Faraday efficiency and the amount of producing H_2 of this working electrode at a current density of 100 mA cm^{-2}.

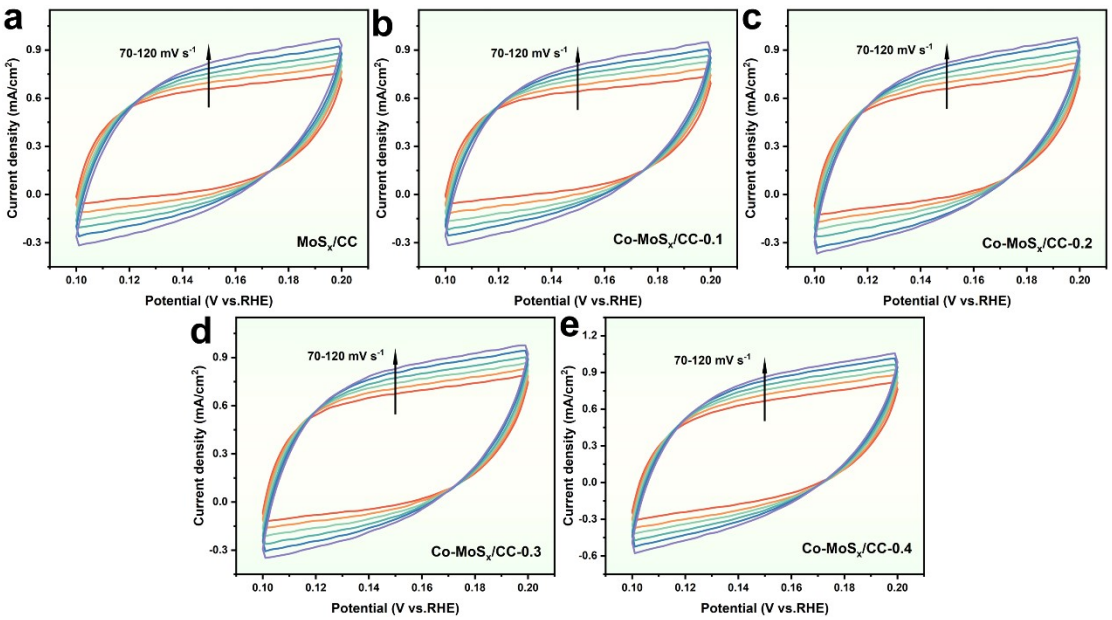

Fig. S25 CV curves of (a) MoS_x/CC, (b) Co–MoS_x/CC–0.1, (c) Co–MoS_x/CC–0.2, (d) Co–MoS_x/CC–0.3 and (e) Co–MoS_x/CC–0.4. Scan rates are 70, 80, 90, 100, 110 and 120 mV s^{-1}, respectively.

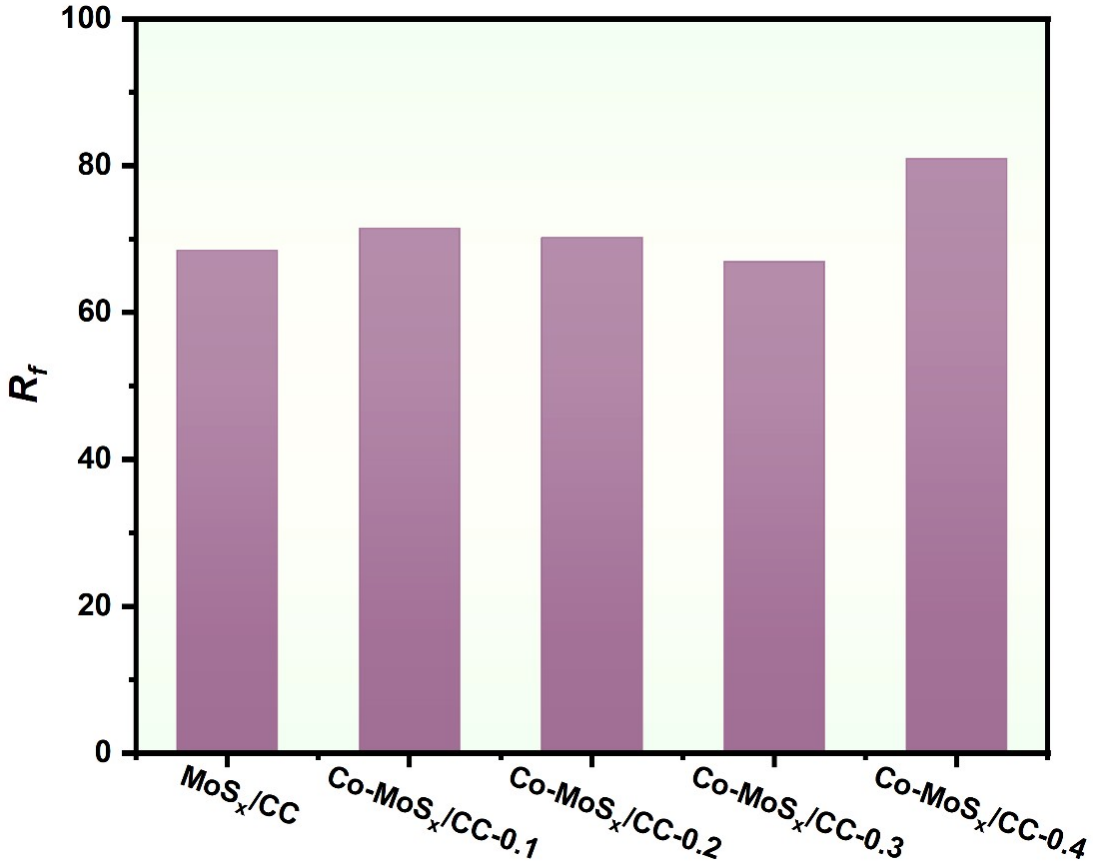

Fig. S26 Roughness factor of MoS_x/CC, Co–MoS_x/CC–0.1, Co–MoS_x/CC–0.2, Co–MoS_x/CC–0.3 and Co–MoS_x/CC–0.4.

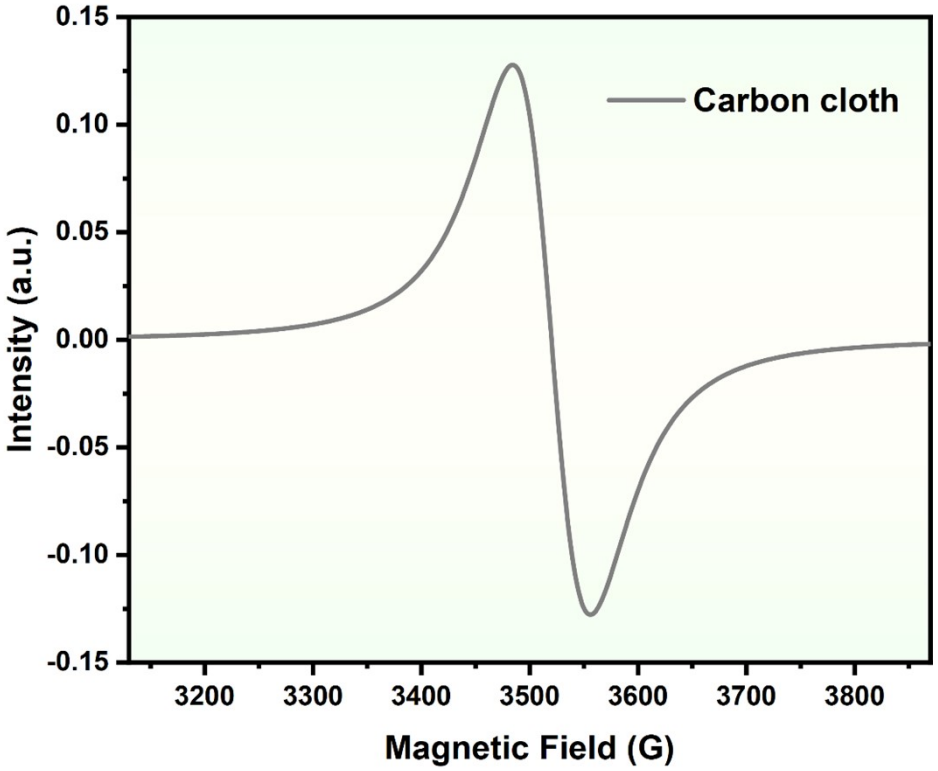

Fig. S27 EPR spectrum of the treated CC.

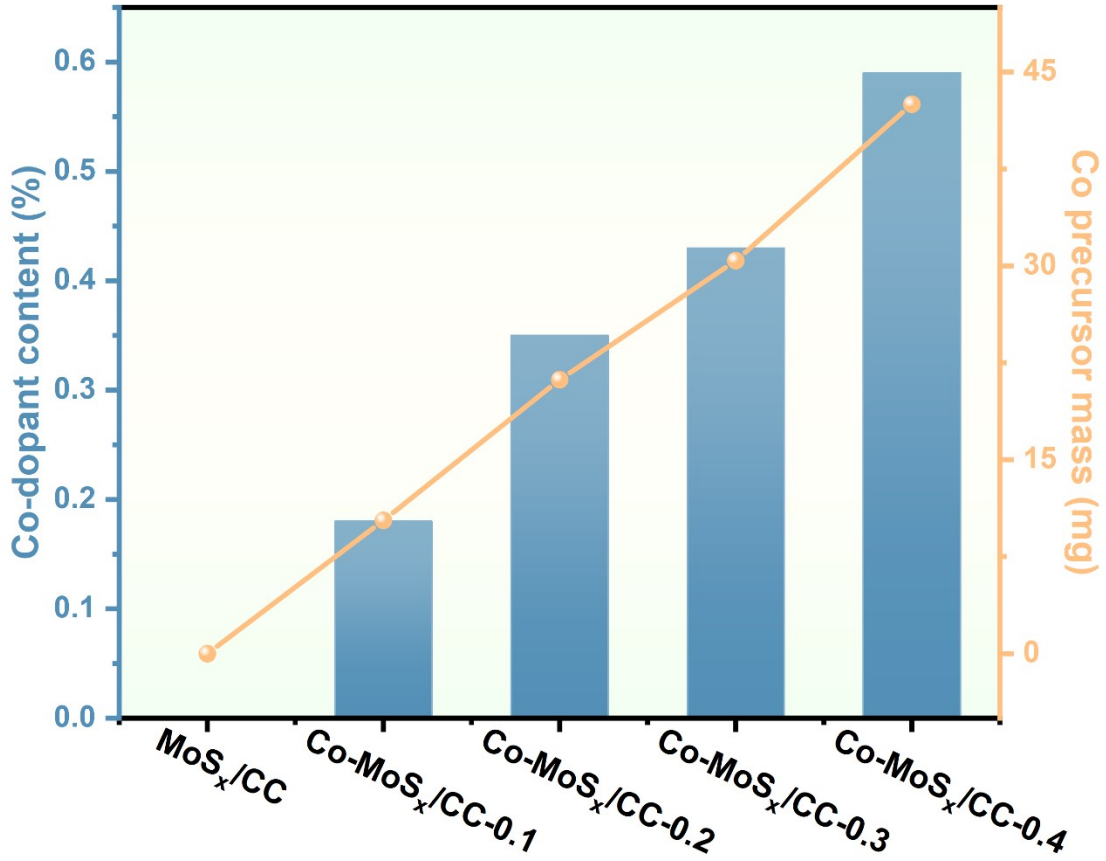

Fig. S28 Co–dopant content of MoS_x/CC, Co–MoS_x/CC–0.1, Co–MoS_x/CC–0.2, Co–MoS_x/CC–0.3 and Co–MoS_x/CC–0.4, as well as the corresponding the mass of Co precursor for the synthesis of MoS_x/CC and a series of Co–MoS_x/CC samples.

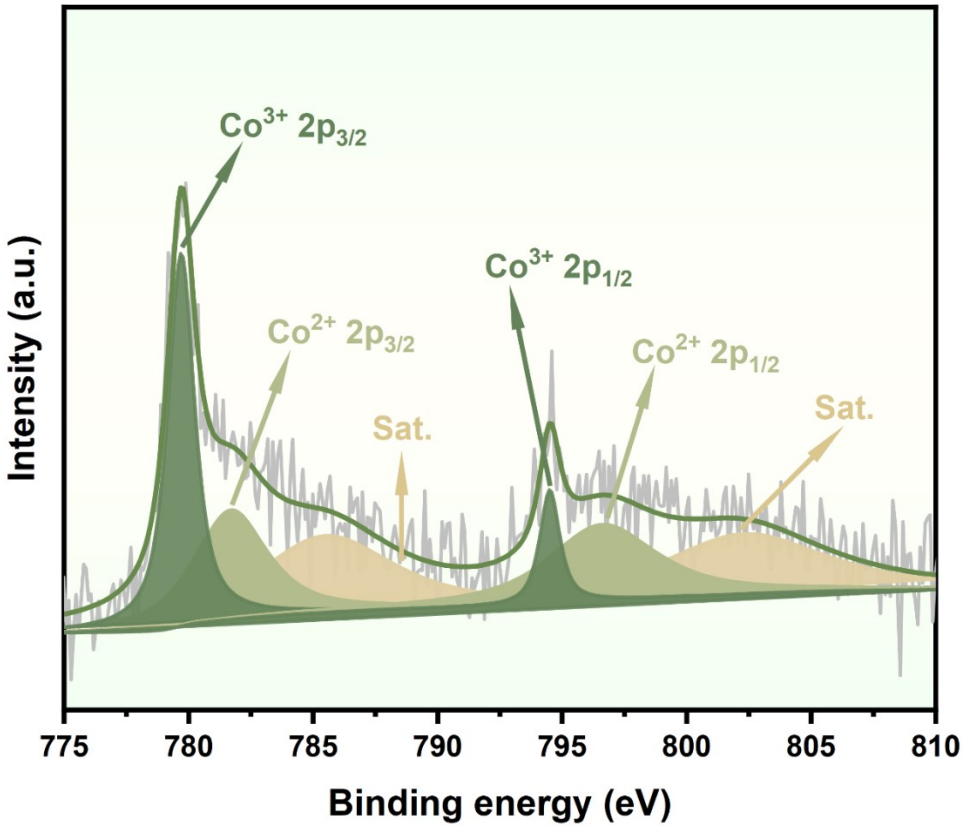

Fig. S29 Co 2p high–resolution XPS spectrum of Co–MoS_x/CC–0.4 in terms of fitting Co^{3+} and Co^{2+} species.

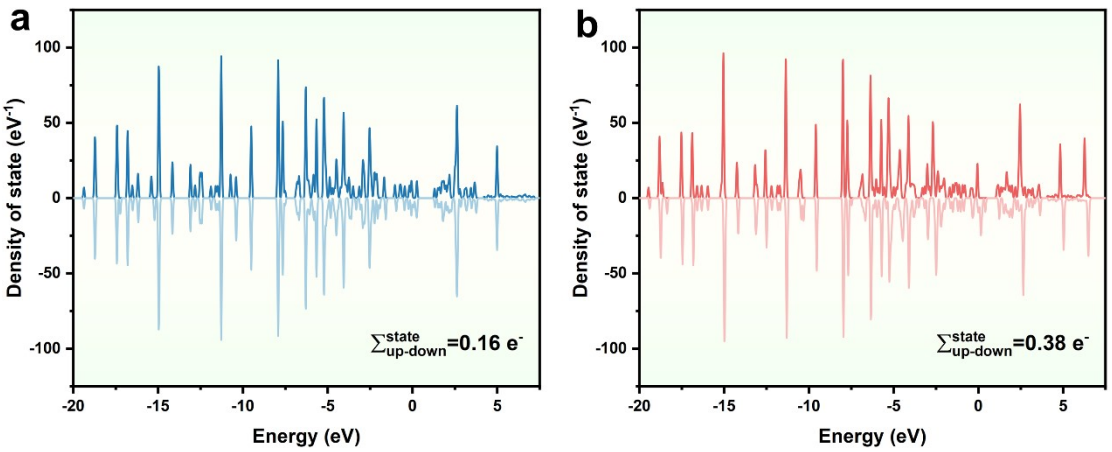

Fig. S30 Density of state (DOS) of (a) MoS_x/CC and (b) Co–MoS_x/CC–type1 models.

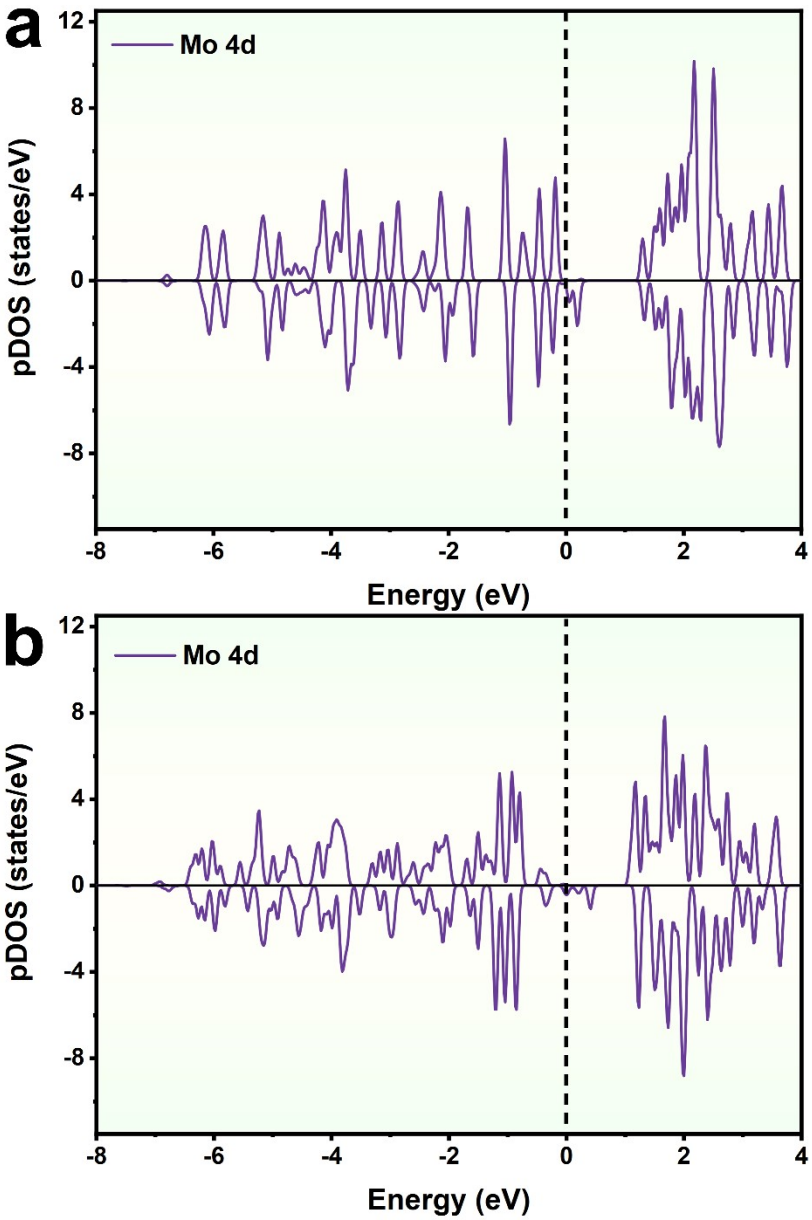

Fig. S31 Projected DOS (PDOS) of Mo 4d in (a) MoS_x/CC and (b) Co–MoS_x/CC–type1 models.

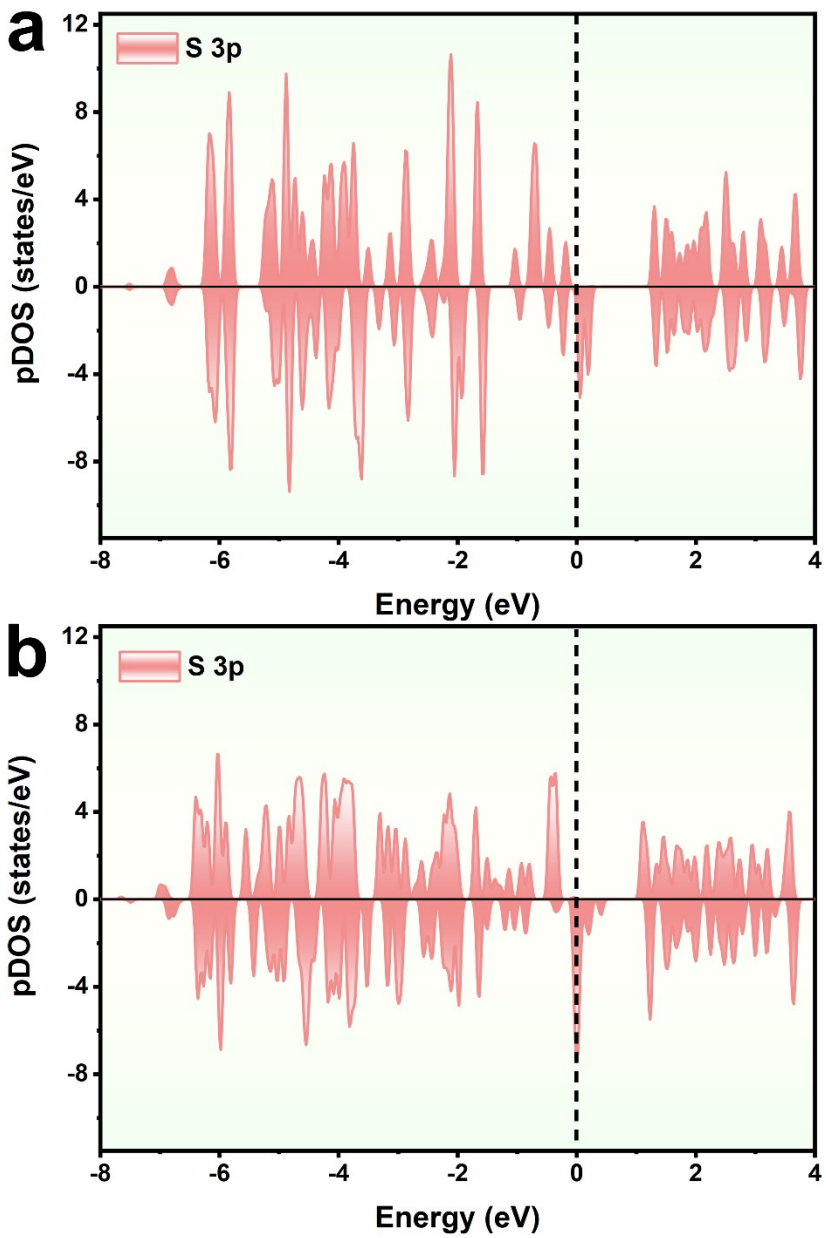

Fig. S32 PDOS of S 3p in (a) MoS_x/CC and (b) Co–MoS_x/CC–type1 models.

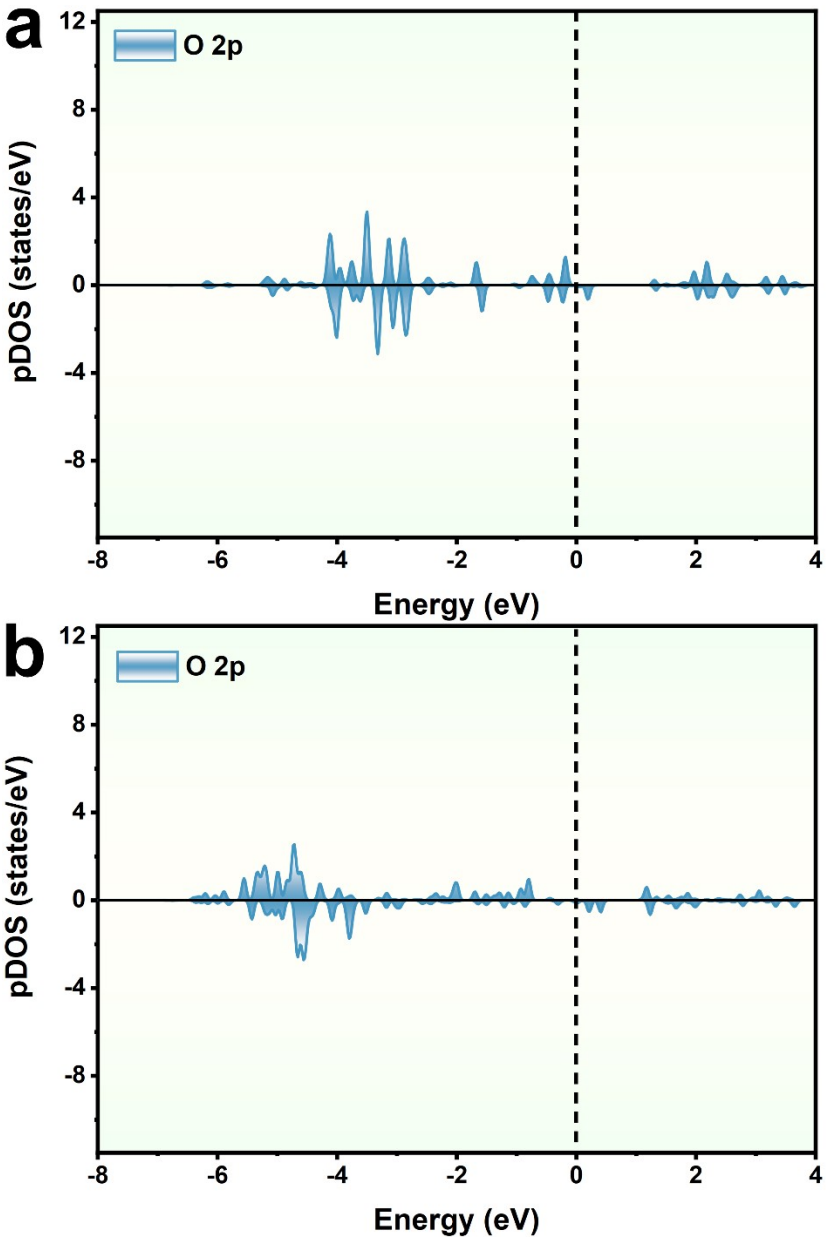

Fig. S33 PDOS of O 2p in (a) MoS_x/CC and (b) Co–MoS_x/CC–type1 models.

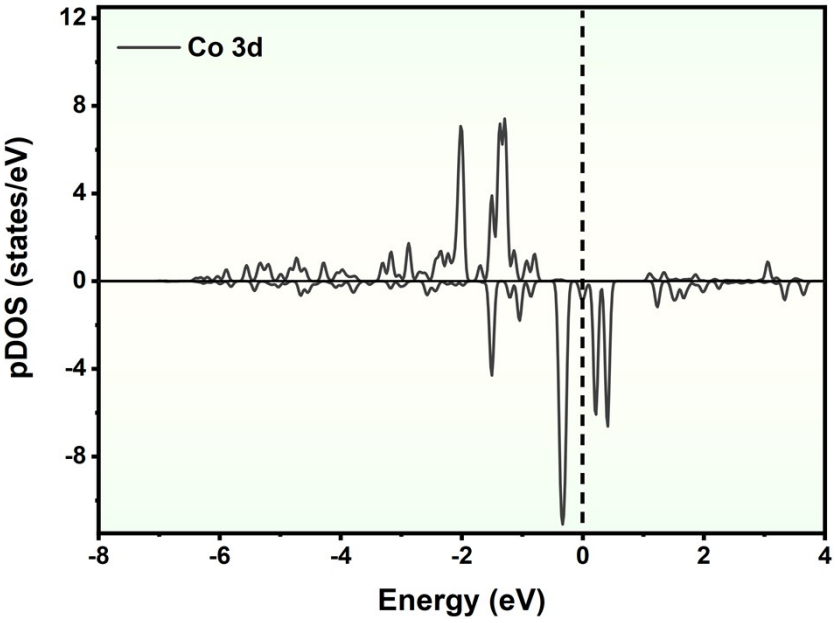

Fig. S34 PDOS of Co 3d in Co–MoS_x/CC–type1 model.

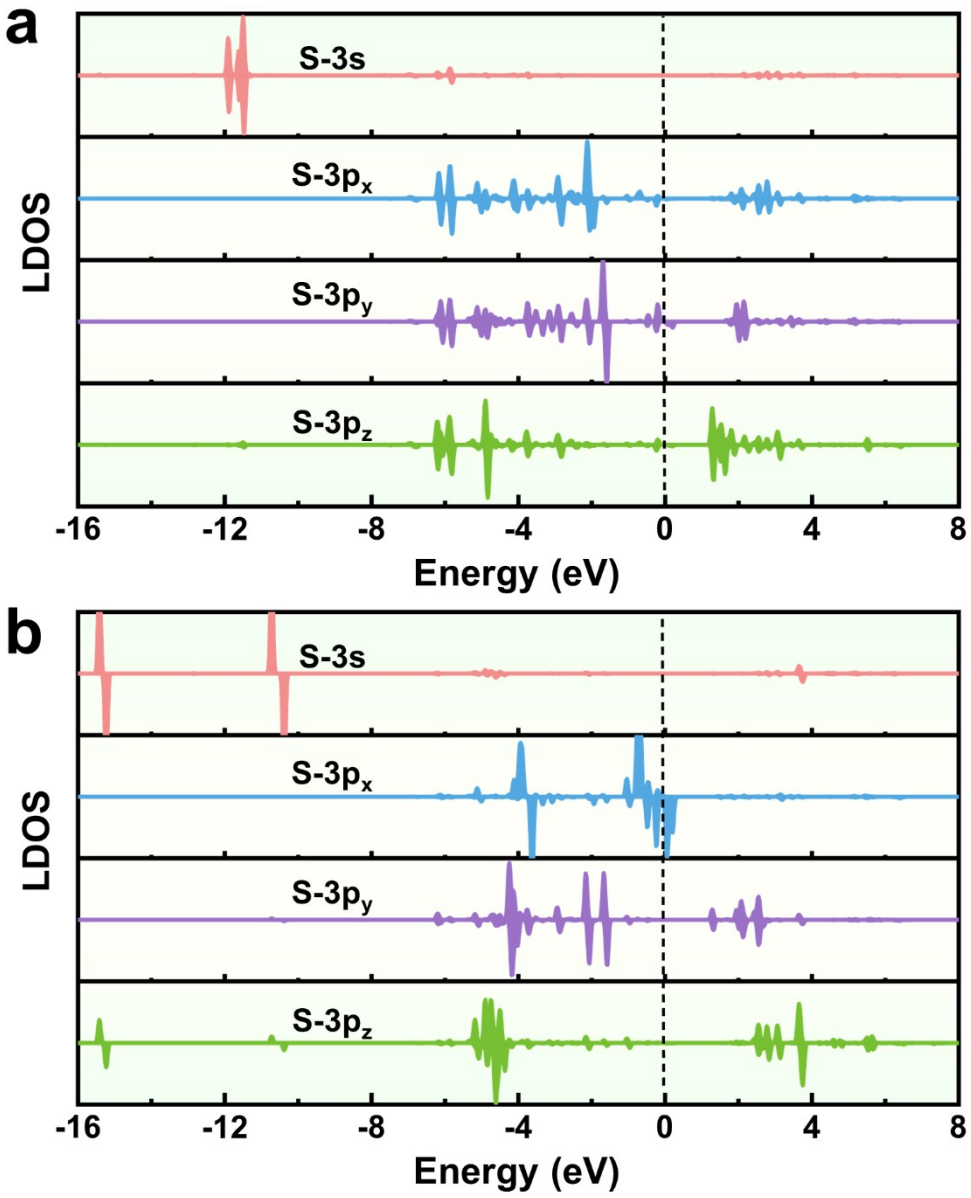

Fig. S35 Local DOS (LDOS) of (a) S1 and (b) S2 sites without hydrogen atom in MoS_x/CC model.

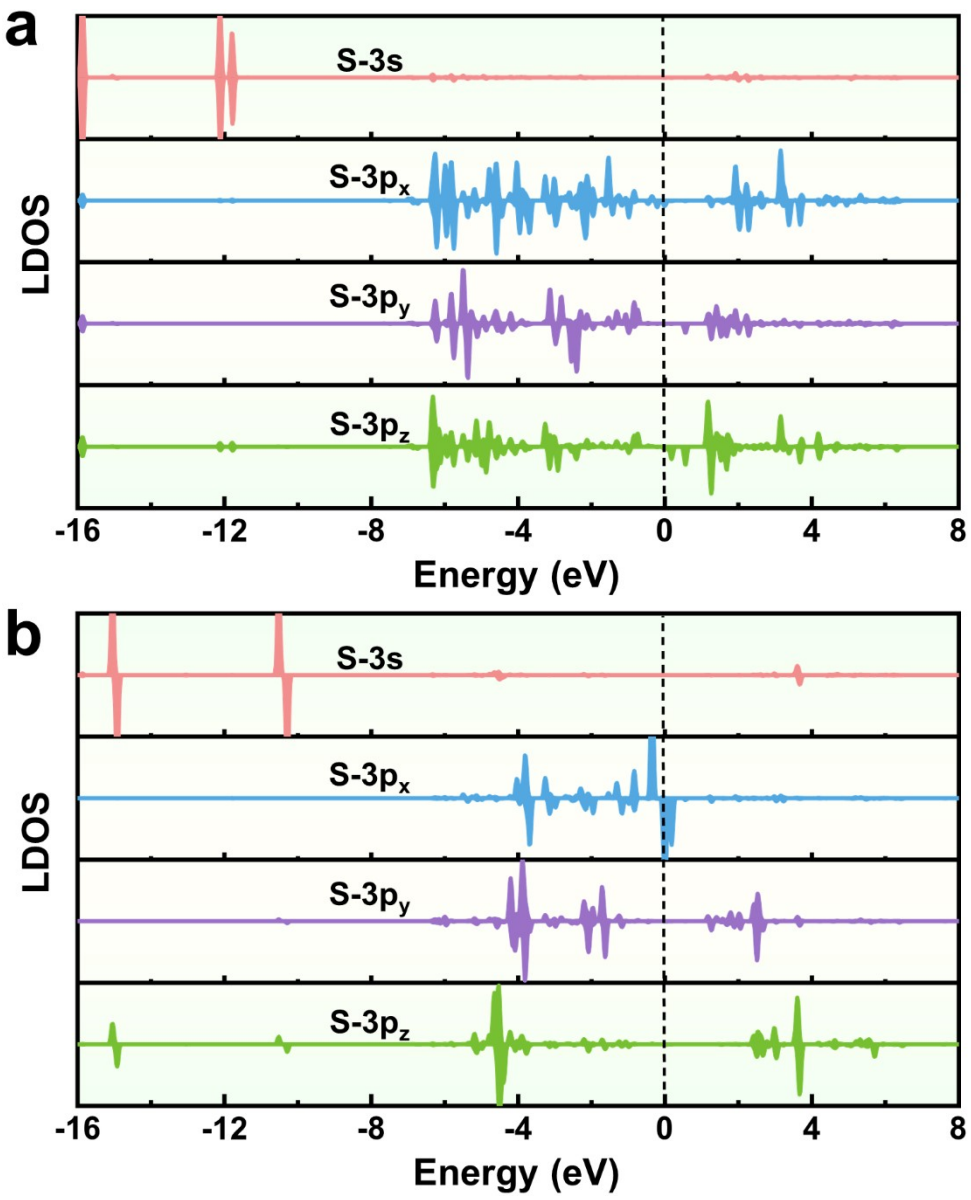

Fig. S36 LDOS of (a) S1 and (b) S2 sites without hydrogen atom in Co–MoS_x/CC–type1 model.

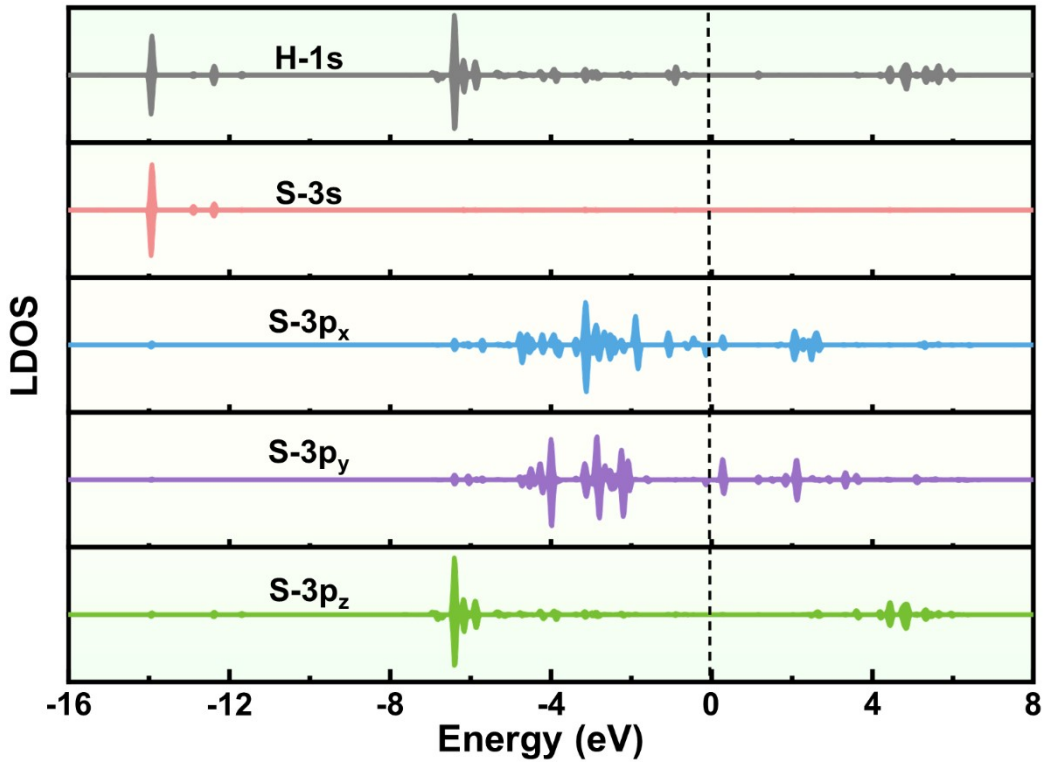

Fig. S37 LDOS of S1 site with hydrogen atom in MoS_x/CC model.

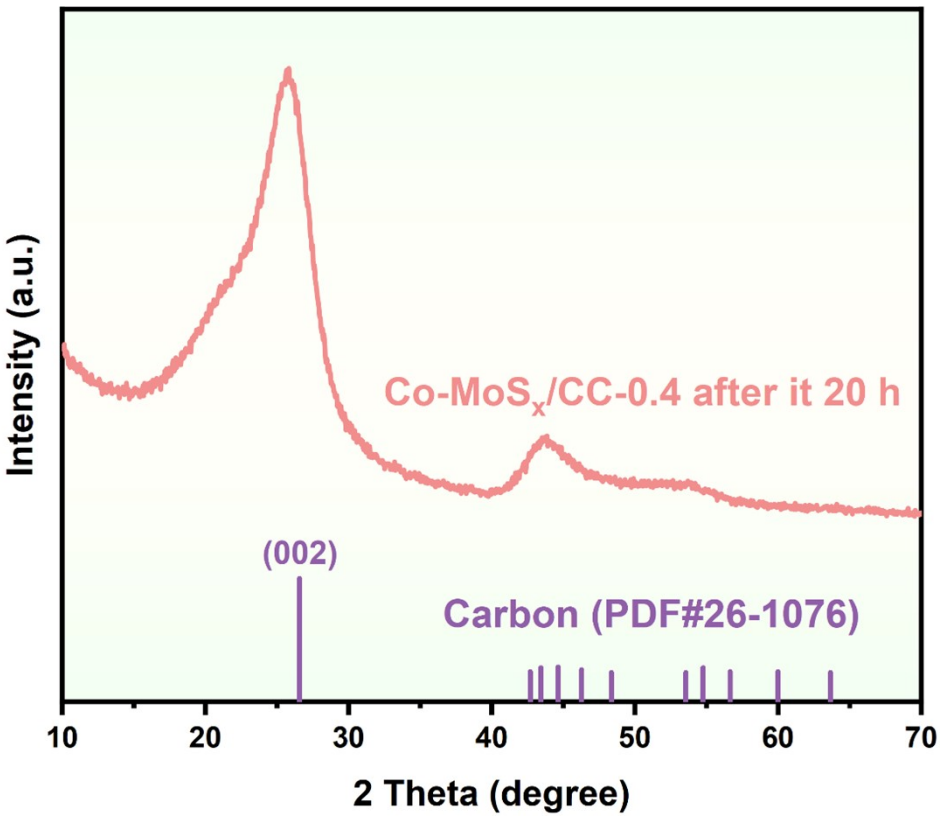

Fig. S38 XRD pattern of Co-MoS_x/CC-0.4 after *i* ~ *t* 20.0 h test.

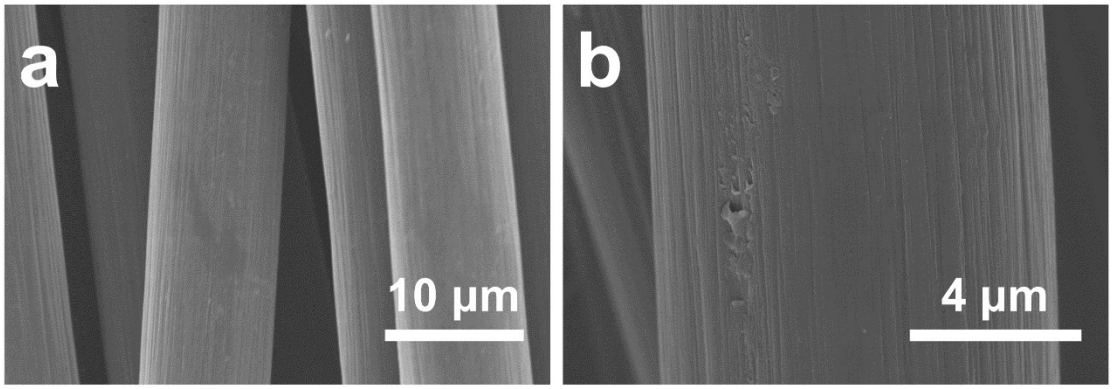

Fig. S39 SEM images of Co-MoS_x/CC-0.4 after 1000 CV cycles.

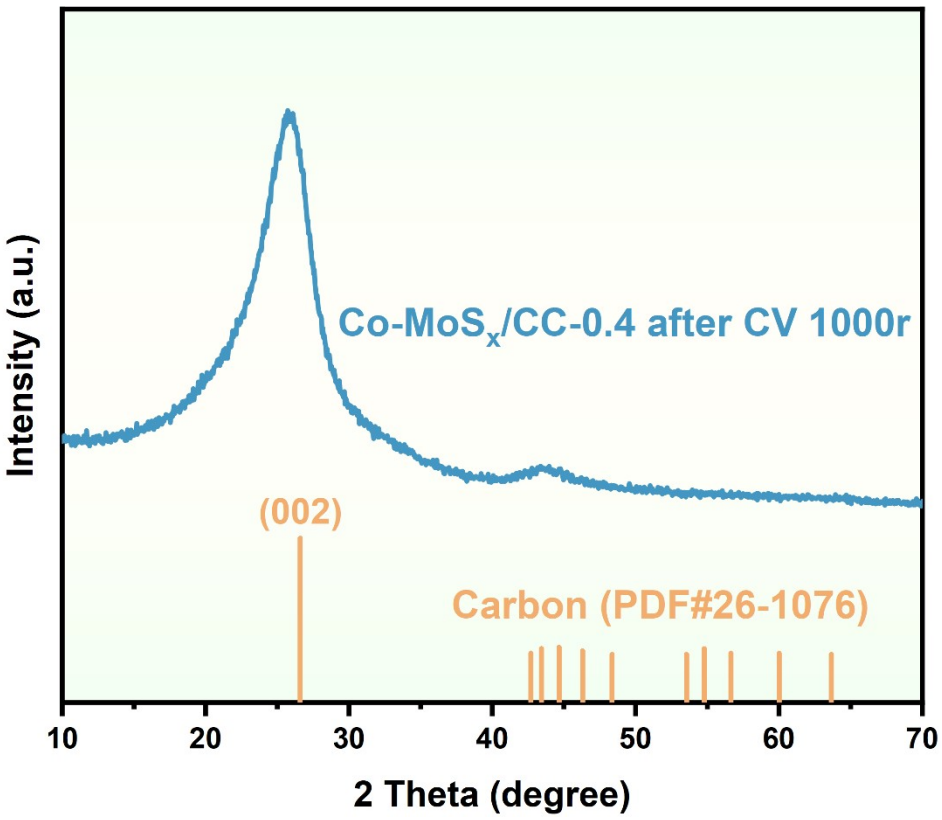

Fig. S40 XRD pattern of Co–MoS_x/CC–0.4 after 1000 CV cycles.

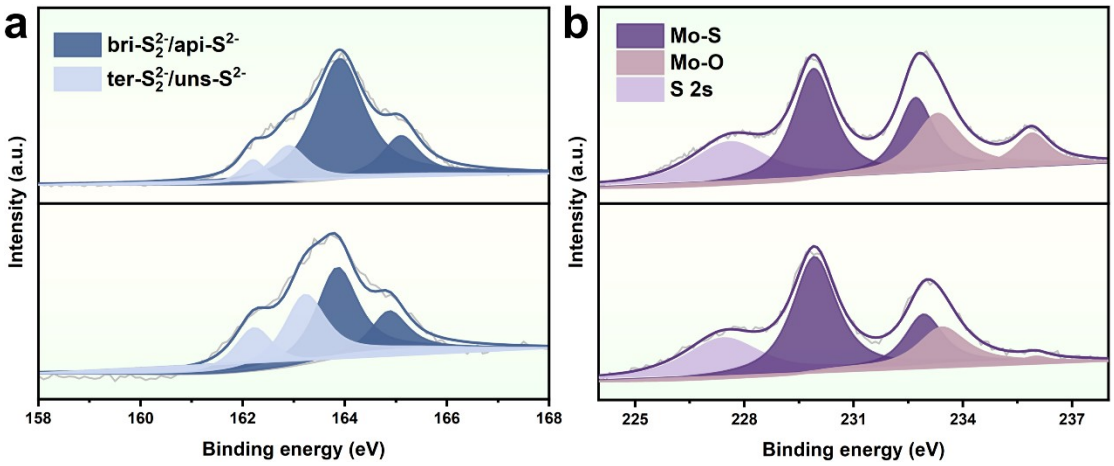

Fig. S41 (a) S2p and (b) Mo3d XPS spectra of Co–MoS_x/CC–0.4 before 1000 CV cycles (upper figure) and after 1000 CV cycles (lower figure).

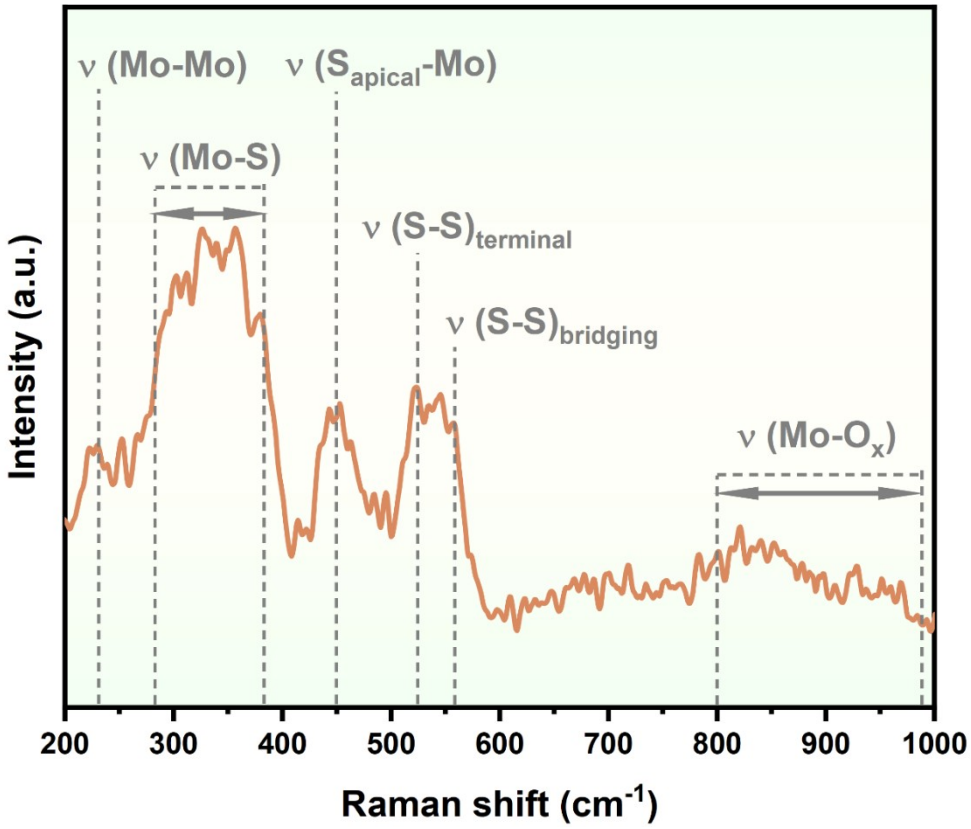

Fig. S42 Raman spectrum of Co–MoS_x/CC–0.4 after 1000 CV cycles.

Table S1 Atom concentrations (*C*) of S, Mo and Co as well as the atom ratios of S and Mo atoms of MoS_x/CC, Co–MoS_x/CC–0.1, Co–MoS_x/CC–0.2, Co–MoS_x/CC–0.3 and Co–MoS_x/CC–0.4.

Samples	*C* of S (%)	*C* of Mo (%)	*C* of Co (%)	S/Mo
MoS_x/CC	33.82	10.64	0.0	3.2
Co–MoS_x/CC–0.1	34.36	10.57	0.18	3.2
Co–MoS_x/CC–0.2	33.78	10.24	0.35	3.3
Co–MoS_x/CC–0.3	27.79	8.32	0.42	3.3
Co–MoS_x/CC–0.4	26.27	7.91	0.54	3.3

Table S2 Calculated formation energies of Co–MoS_x/CC–type1 and Co–MoS_x/CC–type2 models.

Models	Formation energy (eV)
Co–MoS_x/CC–type1	-766.3
Co–MoS_x/CC–type2	-765.8

Table S3 ΔG_{H^*} at S1, S2, Mo1, Mo2 and Co sites of MoS_x/CC and Co–MoS_x/CC–type1 models for HER.

Models	Site	*E*(surface+H)	*E*(surface)	*E*(H_2)	Δ*E*(ads)	ΔG_{H^*}
MoS_x/CC	S1	-763.877	-760.709	-6.771	0.218	0.458
	S2	-764.117	-760.709	-6.771	-0.023	0.217
	Mo1	-763.429	-760.709	-6.771	0.666	0.906
	Mo2	-763.210	-760.709	-6.771	0.885	1.125
Co–MoS_x/CC–type1	S1	-770.067	-766.289	-6.771	-0.393	-0.153
	S2	-769.880	-766.289	-6.771	-0.206	0.034
	Mo1	-768.916	-766.289	-6.771	0.759	0.999
	Mo2	-768.880	-766.289	-6.771	0.795	1.035
	Co	-769.514	-766.289	-6.771	0.161	0.401

Unit: eV.

Table S4 EXAFS fitting results for the local structure parameters around Mo.

Samples	Shell	CN [a]	R(Å) [b]	ΔE_0(eV) [c]	σ^2(10^{-3} Å^2) [d]	R factor(10^{-2}) [e]
Mo foil	Mo-Mo	8	2.72	–	–	–
MoS_x	Mo-S	4.1	2.41	-3.9	3.6	1.7
	Mo-O	1.6	1.97		4.8	
Co–MoS_x–0.4	Mo-S	3.2	2.37	-8.6	2.5	1.8
	Mo-O	1.1	1.95		9.4	

[a] CN: coordination number; [b] R: distance between absorber and backscatter atoms; [c] ΔE_0: inner potential correction; [d] σ^2: Debye-Waller factor to account for both thermal and structural disorders; [e] R-factor indicates the goodness of fit. During data processing, S_0^2 is fixed as 0.976 according to the experimental EXAFS fit of Mo foil by fixing CN as the known crystallographic value. Error range of CN and σ^2 are both 20 %, and the accuracy of R is ± 0.03 Å. Reasonable EXAFS fitting parameters are as follows: $0.7 \leq S_0^2 \leq 1.000$; $\sigma^2 \leq 0.01$ Å^2; $|\Delta E_0| \leq 10$ eV and R factor < 0.02.

Table S5 EXAFS fitting results for the local structure parameters around Co.

Samples	Shell	CN [a]	R(Å) [b]	ΔE_0(eV) [c]	σ^2(10^{-3} Å^2) [d]	R factor(10^{-2}) [e]
Co foil	Co-Co	12	2.52	–	–	–
Co–MoS_x–0.4	Co-S	0.9	2.14	-6.5	3.5	0.9
	Co-O	5.3	1.77		5.4	

[a] CN: coordination number; [b] R: distance between absorber and backscatter atoms; [c] ΔE_0: inner potential correction; [d] σ^2: Debye-Waller factor to account for both thermal and structural disorders; [e] R-factor indicates the goodness of fit. During data processing, S_0^2 is fixed as 0.718 according to the experimental EXAFS fit of Co foil by fixing CN as the known crystallographic value. Error range of CN and σ^2 are both 20 %, and the accuracy of R is ± 0.03 Å. Reasonable EXAFS fitting parameters are as follows: $0.7 \leq S_0^2 \leq 1.000$; $\sigma^2 \leq 0.01$ Å^2; $|\Delta E_0| \leq 10$ eV and R factor < 0.02.

Table S6 Calculated magnetic moments of (1) the MoS_x nanocluster in MoS_x/CC model and (2) the Co–doped MoS_x nanocluster in Co–MoS_x/CC–type1 model.

Models	Magnetic moments (μ_B)
(1)	1.89
(2)	6.74

Table S7 The related bond angles in MoS_x/CC and Co–MoS_x/CC–type1 models.

Models	Angle of O-Mo1-S3	Angle of Mo1-S3-S1
MoS_x/CC	117.8 °	69.9 °
Co–MoS_x/CC–type1	118.5 °	84.5 °

S3 sites indicated in Fig. 4g and 4h are another bri–S_2^{2-} atom, being linked to the S1 site in the $[Mo_3S_{13}]^{2-}$ nanocluster.

Table S8 Comparison of HER activity of Co-MoS_x/CC-0.4 with other molybdenum sulfide-based electrocatalysts reported in the literature.

Samples	Overpotential (mV)@current density (mA cm^{-2})	References
1T MoS_2 nanosheets	-187@10	[7]
wet-chemical-synthesized a-MoS_x	-200@10	[8]
$MoWS_x$/BPE_{anodic}	-278@10	[9]
MoS_x@NbS_2/GC	-164@10	[10]
$CoMoS_x$ NPs (1/2)	-188@10	[11]
MoS_2/C_{800}	-207@10	[12]
MoS_2/g-C_3N_4	-260@10	[13]
MoS_x flat boxes	-206@10	[14]
a-MoS_2/CC	-224@10	[15]
Co_9S_8@MoS_2/CNFs	-190@10	[16]
MoS_x/GO_2	-180@10	[17]
MoS_x/PP-CFP	-205@10	[18]
MoO_2-MoS_x-12	-210@10	[19]
Cu foam@MoS_x	-200@10 -250@100	[20]
Co-MoS_x/CC-0.4	-178@10 -229@100	This work

Table S9 The related Mo-S bond lengths of MoS_x/CC and Co-MoS_x/CC-type1

models.

Models	Ter–S_2^{2-}	Api–S^{2-}	Bri–S_2^{2-}	Average
MoS_x/CC	2.44	2.39	2.47	2.45
Co-MoS_x/CC-type1	2.45	2.37	2.46	2.44

Ter–S_2^{2-}, Api–S^{2-} and Bri–S_2^{2-} designate the related Mo–S bonds. Furthermore, Ter–S_2^{2-}, Api–S^{2-} and Bri–S_2^{2-} indicate that the terminal, apical and bridging S atoms are bonded with Mo atoms, respectively. Average displays the average values of three kinds of Mo–S bond lengths of MoS_x/CC and Co–MoS_x/CC–type1 models.

Unit: Å.

References

1 G. Kresse and J. Furthmüller, *Comp. Mater. Sci.*, 1996, **6**, 15-50.

2 G. Kresse and D. Joubert, *Phys. Rev. B*, 1999, **59**, 1758-1775.

3 J. P. Perdew, K. Burke and M. Ernzerhof, *Phys. Rev. Lett.*, 1996, **77**, 3865-3868.

4 P. E. Blöchl, *Phys. Rev. B*, 1994, **50**, 17953-17979.

5 S. Grimme, J. Antony, S. Ehrlich and H. Krieg, *J. Chem. Phys.*, 2010, **132**, 154104.

6 S. Grimme, *J. Comput. Chem.*, 2006, **27**, 1787-1799.

7 M. A. Lukowski, A. S. Daniel, F. Meng, A. Forticaux, L. Li and S. Jin, *J. Am. Chem. Soc.*, 2013, **135**, 10274-10277.

8 J. D. Benck, Z. Chen, L. Y. Kuritzky, A. J. Forman and T. F. Jaramillo, *ACS Catal.*, 2012, **2**, 1916-1923.

9 S. M. Tan and M. Pumera, *ACS Appl. Mater. Interfaces*, 2017, **9**, 41955-41964.

10 X. Zhou, S. H. Lin, X. Yang, H. Li, M. N. Hedhili, L. J. Li, W. Zhang and Y. Shi, *Nanoscale*, 2018, **10**, 3444-3450.

11 L. Gan, J. Liu, Y. Ren, Z. Xiong, K. Chen and Y. Zhao, *Carbon Lett.*, 2023, **33**, 1367-1380.

12 H. Sun, X. Ji, Y. Qiu, Y. Zhang, Z. Ma, G. G. Gao and P. Hu, *J. Alloys Compd.*, 2019, **777**, 514-523.

13 P. Fageria, K. Y. Sudharshan, R. Nazir, M. Basu and S. Pande,

Electrochim. Acta, 2017, **258**, 1273-1283.

14 L. Chen and H. Zhu, *ChemCatChem*, 2018, **10**, 459-464.

15 X. Zhang, Y. Zhang, B. B. Yu, X. L. Yin, W. J. Jiang, Y. Jiang, J. S. Hu and L. J. Wan, *J. Mater. Chem. A*, 2015, **3**, 19277-19281.

16 H. Zhu, J. Zhang, R. Yanzhang, M. Du, Q. Wang, G. Gao, J. Wu, G. Wu, M. Zhang, B. Liu, J. Yao and X. Zhang, *Adv. Mater.*, 2015, **27**, 4752-4759.

17 W. H. Hu, X. Shang, G. Q. Han, B. Dong, Y. R. Liu, X. Li, Y. M. Chai, Y. Q. Liu and C. G. Liu, *Carbon*, 2016, **100**, 236-242.

18 R. Bose, S. K. Balasingam, S. Shin, Z. Jin, D. H. Kwon, Y. Jun and Y. S. Min, *Langmuir*, 2015, **31**, 5220-5227.

19 Y. Qiu, L. Chai, Y. Su, P. Li, W. Yuan, H. Li and X. Guo, *Dalton Trans.*, 2018, **47**, 6041-6048.

20 S. Min, J. Qin, W. Hai, Y. Lei, J. Hou and F. Wang, *Int. J. Hydrogen Energy*, 2018, **43**, 4978-4986.